PONTIFICIA UNIVERSIDAD CATÓLICA DEL PERÚ

GRADUATE SCHOOL

The AD detector array: a new tool for studying diffractive physics at the ALICE experiment

Thesis submitted to obtain the degree of Master of Science in Physics:

Ernesto Calvo Villar

ADVISOR: Dr. Alberto Gago Medina

Lima, Jan 2015

The AD detector array: a new tool for studying diffractive physics at the ALICE experiment

Ernesto Calvo Villar

Submitted to obtain the degree of Master of Science in Physics
2015

Abstract

We present a new detector array proposal for the ALICE experiment at LHC. This new subdetector is composed of four stations of scintillator pads and its main goal is to extend our current rapidity coverage. Therefore, we would have more sensitivity to tag the rapidity gaps related to the diffractive processes.

In particular, we show a study of the performance of this new subdetector and its impact in our ability to select diffractive events. Certainly, this new system will contribute to improve the ALICE capabilities in addressing several subjects on diffractive physics.

Acknowledgments

I would like to thank my advisor, Dr. Alberto Gago, for his encouragement and patience during the entire period of this work. To Rodrigo Helaconde for useful help with Pythia6 and Phojet generation. Also, Joel Jones and Eric Endress, for useful suggestions about this work.

To Jean-Pierre Revol, Martin Poghosyan and all the members of the AD group, for the great experience of developing a new detector for the ALICE experiment at the LHC.

This project would have been impossible without the computational power provided by Legion, a grid-like supercomputer facility developed by the 'Dirección de Informática Académica' (DIA). Special thanks are due to Genghis Rios and Oscar Díaz for developing Legion in the first place, and for their great and continuous support.

To my friends, Jose, Claudia, Giulliana, for the great adventures we have been through. To Carmen, for always having a kind advice when I needed one. And Darling, for bringing a smile to my face.

Finally, I would like to thanks my parents, Alfredo and Isabel, for all the sacrifices they made for me. And to my brother and sister, who somehow forgave me for being a physicist and an older brother.

Contents

List of Figures

List of Tables

Chapter 1

Introduction

1.1 The ALICE experiment

A Large Ion Collider Experiment (ALICE) is one of the seven experiments of the Large Hadron Collider (LHC) which is located in the Franco-Swiss border and run by the *European Organization for Nuclear Research* (CERN). Its main physics goal is the study and characterization of a new state of matter known as *quark-gluon plasma* (QGP) created in high energy heavy-ion collisions. Quarks in normal conditions are inextricably locked into the hadrons they belong, but become deconfined in this new state, forming a high density, low viscosity fluid in which they are almost free to move, and where there are no more hadronic boundaries.

To this end, ALICE participates in dedicated lead-lead runs at the LHC at a center of mass energy (CMS) per nucleon of $\sqrt{S_{NN}} = 2.76$ TeV for the study of key QGP Observables. ALICE also collects data from proton-proton runs at an CMS energy of $\sqrt{S} = 7$ TeV in order to disentangle true QGP behavior from what could be a simple consequence of the scaling in the number of participant nucleons.

In addition to this, special p+Pb runs were performed at the end of 2012 and beginning of 2013 from which ALICE certainly profited as this allowed to confirm that observations made in Pb+Pb collisions originate from the presence of QGP.

ALICE is unique among other experiments at the LHC due to its excellent particle identification capabilities, low transverse momentum p_T threshold, and their coverage in eight units of pseudorapidity. In the following sections we describe briefly the main sub system of ALICE.

1.1.1 Solenoid Magnet

Most of the ALICE experiment detectors are surrounded by a big solenoid producing a magnetic field of 0.5 Tesla in the beam (or z) direction. The purpose of this magnetic field is to help the detectors in the central region of ALICE to identify the charged particles by measuring the bending of their path caused by the Lorentz force.

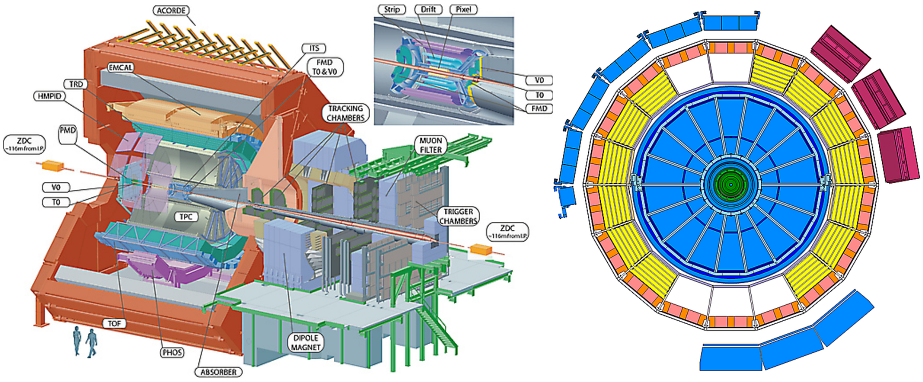

Figure 1.1: The ALICE experiment at CERN. Left: 3D view showing the diferent subdetectors and the L3 solenoid magnet (in red). Right: Cross section showing installed detectors as of 2012.

1.1.2 Central Tracking Detectors

Time Projection Chamber (TPC)

The TPC is the main tracking device of ALICE. It is able to reconstruct the three-dimensional path of the charged particles that traverse its volume and allows for charged particle momentum measurements (through the bending of the track in the ALICE solenoid magnetic field), charged particle identification (via dE/dx measurements), track reconstruction and vertex determination.

The TPC consists of a cylindrical chamber with its symmetry axis oriented parallel to the beam pipe (fig. 1.2) and filled with a Ne/CO$_2$/N$_2$ (85.7%/9.5%/4.8%) gas mixture at atmospheric pressure. Inside the TPC, a thin foil electrode located at its center divides the TPC in two halves. A difference of potential is applied between this electrode and the end caps creating an electric field parallel to the z axis. In addition to the electric field, the external solenoid magnet of ALICE creates a magnetic field of 0.5 Tesla parallel to the TPC axis.

The principle of operation of the TPC is the following [13]: When a charged particle traverse the volume of the TPC, it ionizes the gas molecules of the medium releasing a trail of electrons and ions. The electrons are then pulled towards the end caps of the TPC due to the electric field (400 V/cm) previously mentioned, leaving a projection in the XY plane of the tracks. Under this combination of field strength, gas mixture and pressure, the maximum drift time of the electrons is of $90\mu s$. During this time the traveling image of the track is broadened by the transverse diffusion of electrons during the drift. Normally this would affect the resolution in the determination of the track. However, in the TPC, the Lorentz force on the drifting electrons (generated by the XY component of their velocity and the axial magnetic field) reduce this effect by forcing the electrons to move in helical paths toward the end caps.

At the end caps of the TPC, the charge is collected by a set of readout pads consisting in Multi-Proportional Wire Chambers (MPWC) with cathode readout. These devices consist of two parallel cathode planes and a middle plane of thin anode wires. The electric field around the wires is stronger closer to the anode wires. As the electrons approach the wires, the electric field becomes strong enough as to produce secondary ionization, i.e, to deliver the required kinetic energy to electrons so that they are able to strip some electrons in their next collision with a gas molecule. This process is repeated over and over generating an amplification by avalanche of the signal. In a cathode readout MPWC the cathode planes are also made of parallel wires oriented perpendicular to the direction of the anode wires allowing an increase in the position resolution.

After this an XY projection of the ionizing track is created in the end caps and the z coordinate is inferred from the arrival time of the electrons. With all this information the TPC is able to make a full 3D reconstruction of the track.

If a the track leaves clusters in ITS, TRD, TOF and TPC it is called a track with full radial length. For these tracks the information from different detectors can be combined to obtain a more accurate particle identification on momentum resolution. The pseudorapidity coverage of TPC in this case is $|\eta| < 0.9$

If we only require the tracks to hit anywhere in the TPC then the pseudorapidity coverage is $|\eta| < 1.5$ (reduced track length). The ALICE TPC is able to observe tracks from low p_T of 0.1 GeV/c up to 100 GeV/c.

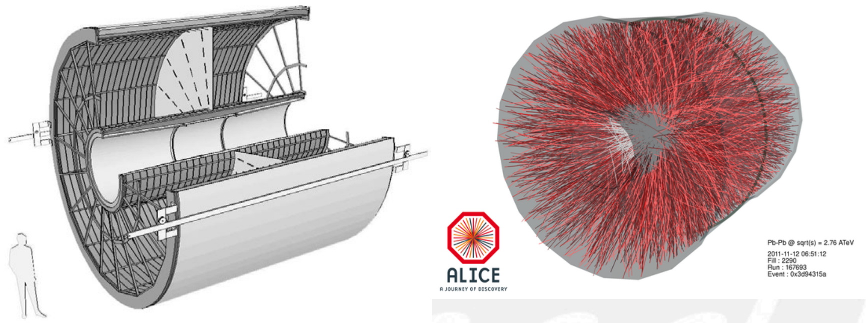

Figure 1.2: The Time Projection Chamber of ALICE. Left: Schematic view (from [6]). Right: Tracks reconstructed by TPC in a Pb-Pb event.

Inner Tracking System (ITS)

The ITS consist of six layers of silicon detectors (fig. 1.3), located at 4, 7, 15, 24, 39 and 44 cm from the beam line. Their mission is the determination of the primary vertex and the tracking and identification of particle with momentum below 100 MeV.

In semiconductor detectors [13] a charged particle traversing a volume of this material will create electron-hole pairs by exciting electrons from the valence band to the conduction band leaving behind a hole in the valence band. The electrons will dissipate their remaining energy by producing more electron-hole pairs (excitons) and by exciting lattice oscillations (phonons). This leaves a zone around the path traversed by the particle with a high concentrations of electrons and holes (10^{15} to 10^{17} per cm^3). In order to get a detectable signal these electrons have to be collected in the anode before they can recombine with the holes.

This can be achieved by using $p - n$ junctions with a reverse bias voltage. A $p - n$ junction is the frontier between a zone in the semiconductor material doped with electron acceptor impurities and another doped with electron donor impurities. When a reverse bias electric field is applied to the p–n junction, a rearrangement of the charge carriers and the valence and conduction bands near the border creates the adequate condition for the collection of charges left by the charged track.

Silicon Pixel Detector (SPD) It makes up the first 2 layers of the ITS. The SPD is made up of 240 ladders, each one with a sensitive area of 12.8mm $(r\varphi) \times 69.6$mm (z). The ladder is a silicon pixel sensor matrix consisting of 256×160 cells, each cell measuring 50 μm in the $r\varphi$ direction and 425 μm in the z direction. Two ladders are mounted along the z axis to form a half-stave. Then, the half-staves are mounted in carbon-fibre supports called sectors. Each sector supports 6 half-staves, two for the inner layer and four for the outer layer. Ten sectors are mounted together around the beam pipe to fully cover the azimuthal angle. So we have 80 ladders for the inner layer of SPD and 160 for the outer layer. This detector is capable of providing fast signal triggers.

Silicon Drift Detectors (SDD) The Silicon Drift Detectors equip the two intermediate layers of the ITS, where the charged particle density is expected to reach up to 7 particles per cm^2. They have a very good multi-track capability and provide dE/dx measurements needed for the ITS particle identification

Silicon Strip Detectors (SSD) The outer layers of the ITS are crucial for the connection of tracks from the TPC to the ITS. They also provide dE/dx information to assist identification of low-momentum particles. Both outer layers consist of double-sided Silicon Strip Detectors (SSD), mounted on carbon-fibre support structures identical to the ones used in SDD.

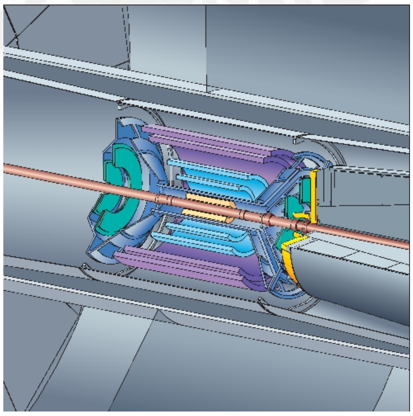

Figure 1.3: The Inner Tracking System of ALICE.

Transition-Radiation Detector (TRD)

The TRD detector (fig. 1.4) surrounds the TPC in the pseudorapidity range $|\eta| \leq 0.9$. The main goal of the TRD is to provide electron identification in the central barrel for particles with momentum greater than 1 GeV/c, where the pion rejection capability through energy loss measurement in the TPC is no longer sufficient. The principle of operation of the TRD is the following:

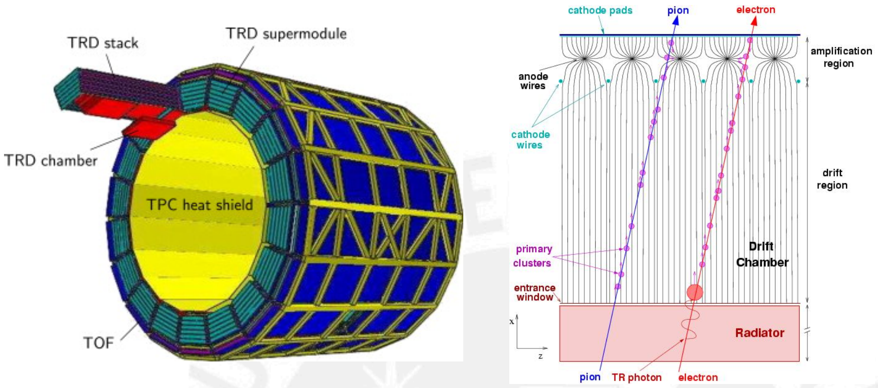

Figure 1.4: The Transition Radiation Detector in ALICE. Left: Schematic view. Right: Principle of operation. Adapted from [7]

When a highly relativistic ($\gamma > 10^3$) charged particle crosses the boundary between two medium of different refraction index (n), a forward cone of soft X-ray photons is produced with a characteristic peak near to the polar angle given by $\phi \approx 1/\gamma$. This is called transition-radiation (TR) and its intensity is proportional to $\gamma = 1/\sqrt{1-\beta^2}$ for a single boundary crossing.

This production can be understood in a qualitative way if we imagine that the particle, while approaching the boundary to the denser medium, forms together with its image, an electric dipole. The field strength of this dipole varies as the particle gets closer to the boundary and vanishes upon entering to the denser medium. The sudden variation in time of the dipole produces the TR radiation.

Since only a few photons are generated in each boundary crossing, multiple layers of radiator materials are typically used. The interference effects from multiple boundary emissions lead to a saturation effect for a Lorentz factor of $\gamma_{\mathrm{SAT}} = 0.6\omega_1\sqrt{l_1 l_2}/c$ where ω_1 is the radiator's plasma frequency, l_1 is its thickness and l_2 is the spacing.

In order to detect the TR photons, a MPWC is commonly placed after the radiator. Since the absorption of X-rays is proportional to $Z^{3.5}$, it is convenient to use a low Z material for the radiator and a gas with high atomic number (for example Xenon, $Z = 54$) for the MPWC detector thus maximizing the conversion of X-ray photons in the detector.

In practice, there will be a superposition of the charge left by the crossing charged particle and the charge coming from the conversion of the X-ray generated at the radiators. Nevertheless, the X-ray photons are quickly absorbed and converted into charge as soon as they enter the MPWC with high Z gas. In this way, tracks from fast particles above the TR threshold ($\gamma \sim 10^3$) will have a characteristic high charge deposit at the beginning in contrast to tracks with the same momentum but higher mass (and hence lower γ). This fact is exploited in order to differentiate a faster electron from a slower pion both with the same momentum.

The TRD fills the radial space between the TPC and TOF detectors (fig. 1.4) and consists of 18 azimuthal sectors each with six radial layers. In the beam direction (z) there is a five fold segmentation giving a total of 540 detector modules each one consisting of a radiator, a multi-wire proportional readout chamber with a gas mixture of Xe/CO_2 (85%/15%), and the frond end electronics for this chamber.

Time Of Flight (TOF)

The Time Of Flight detector uses the Multi gap Resistive Plate Chambers (MRPC) technology. This is an evolution of the Resistive Plate Chamber (RPC) which in turns originated from the spark chamber. The spark chambers where usually made of two planar parallel plates with a high voltage applied to them and the gap between them filled with a gas mixture. When a charged particle traverse the detector it leaves a trail of ionized particles (primary ionization) in the gas mixture. This charges are accelerated by the high voltage to the point where the kinetic energy they gain between successive collisions with gas molecules is enough to cause further ionization on the medium (avalanche). As the avalanche progress, it reaches a size in which the photons coming from the recombination contribute to the creation of more free charges, at this point the avalanche becomes a stream. At a later stage, a conducting plasma filament connecting the two electrodes is formed and a spark is created discharging the electrodes. This has the advantage that the rapidly growing current in the anode could be transformed in a fast voltage signal without the need of further amplification allowing a time resolution of around 1 ns. The drawback was the need for a switching off circuit to prevent the discharge to permanently short circuit the spark chamber, leading to dead times of about 1 second. Also as the area of the chamber increases the energy of the spark becomes large enough as to be able to damage the chamber, so most chambers were restricted to area sizes of a few cm^2.

The RPC was developed to overcome this problems. The electrodes are made of parallel high resistivity (10^9 to $10^{13}\Omega\text{cm}$) material with a few millimeters gap between them filled with a gas chosen to absorb UV photons in order to prevent the transverse grow of discharges. The back of the electrodes are coated with a low resistivity ($\sim 10^5\Omega\text{cm}$) material which are maintained at a high voltage. The passage of charged particles initiates a charge flow to the anode but due to its high resistivity, the charge accumulates in a small region of it causing the local voltage to drop below the level necessary to maintain the discharge. The sensitivity of the detector outside this region is unaffected. When used in avalanche mode this device can sustain rates of up to 1kHz/cm^2. Nevertheless this mode of operation requires the primary ionization to take place near the cathode for the avalanche process to be able to amplify the signal to a detectable level. Thus to increase the efficiency of this process, larger gaps are required. This however will increase the uncertainty in the arrival time of the signal reducing the time resolution.

The MRPC tries to maintain the advantages of the RPC while increasing the efficiency and time resolution. This is achieved by placing thin dielectric sheets between the resistive plate electrodes, creating several thin gaps. In order to compensate for the smaller gaps, a gas mixture producing more ionization clusters per track length is selected. This dielectric sheets then will be polarized due to the electrostatic field and the whole device will behave as several thin RPC parallel to each other. The smaller gaps improve the time resolution and the efficiency is maintained by tune of the gas mixture and by the fact that a charged particle will pass trough several active regions increasing the probability of get a detectable signal.

The Time Of Flight detector in ALICE covers the central pseudo-rapidity region ($|\eta| < 0.9$) for particle identification in the intermediate momentum range (from 0.2 to 2.5 GeV/c). Since the majority of the produced charged particles is emitted in this range, the performance of this detector is of crucial importance for the experiment.

High Momentum Particle Identification Detector (HMPID)

The HMPID provides the inclusive measurement of identified hadrons for $pT >$ 1 GeV/c. It will enhance the particle identification (PID) capabilities of the ALICE experiment by enabling identification of particles beyond the momentum interval attainable through energy loss (ITS and TPC) and time of flight measurements (TOF). The detector was optimized to extend the useful range for π/K and K/p discrimination, on a track-by-track basis, up to 3 and 5 GeV/c respectively.

1.1.3 Forward Detectors

VZERO

The VZERO system is composed of two arrays of scintillator pads located at -90 cm (V0-C) and 330 cm (V0-A) from the interaction point, covering the pseudorapidity ranges $-3.7 < \eta < -1.7$ and $2.8 < \eta < 5.1$ respectively. Each station is segmented in four rings each divided in eight sectors in the azimuthal direction making a total of 32 modules per station. Each module or pad is read out by one photomultiplier.

The principle of operation is the following. When charged particles hit the plastic scintillators, they cause the excitation of the molecular levels in the organic material. After a short time (typically in the range of nano seconds) these excited states decay and light in the ultraviolet region of spectrum is produced. Most organic scintillators transparent to visible light are not transparent in the ultraviolet band (absorption length in the range of a few millimeters), therefore, it is necessary to introduce a second fluorescent substance that converts the ultraviolet photons to photons with a frequency that is not so strongly absorbed by the material (i.e. to avoid re-absorption). Then, this light is collected and directed to the photo cathode of the photomultiplier tube (PMT) where the light will be converted into electronic signal. In the PMT, the photons that hit the photocathode generate electrons via the photoelectric effect. These electrons are then directed and accelerated (via a high potential differences) toward structures called dynodes. When the electrons hit a dynode, they generate more electrons via secondary emission, thus amplifying the signal. This secondary electrons are then directed toward another dynode where they are further amplified. This process is repeated as the electrons pass from dynode to dynode making possible a big amplification of the electronic signal. Scintillation systems based in organic material are able to produce very fast signals and are able to indicate with very good time resolution the time of passage of first particles (leading time)

In particular, for the VZERO array the average time resolution per channel is of the order of one nanosecond [1] The core function of the VZERO detector is to provide fast trigger signals to the selection of an interaction event (Minimum Bias trigger) and the determination of basic physics quantities such as luminosity, particle multiplicity, centrality (for proton-proton and Pb-Pb collisions) and event plane direction in nucleus-nucleus collisions.

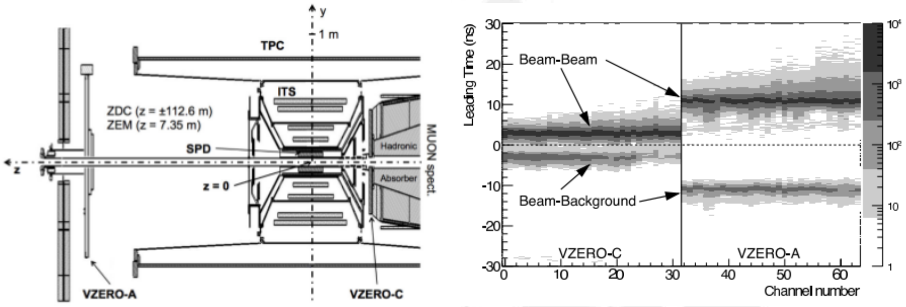

Figure 1.5: The VZERO detectors in ALICE. Left: Schematic view. Right: Rejection of beam-gas background based on timing signals. Adapted from [1]

Furthermore, timing signals from both VZERO's can be used to detect background events coming from beam-gas interactions originating outside the region between the V0-A and V0-C. As can be seen in fig. 1.5, the high resolution in the leading time determination allows the VZERO arrays to separate very well events due to beam-beam events from those with contamination from by beam-gas interactions.

Forward Multiplicity Detector (FMD)

The FMD consists of silicon strip sensor with around 5×10^4 active detection elements, arranged in five rings perpendicular to the beam direction, covering the pseudorapidity ranges $-3.4 < \eta < -1.7$ (FMD-3) and $1.7 < \eta < 5.1$ (FMD-1 and FMD-2). Its main functionality is to provide (offline) charged-particle multiplicity information.

Muon spectrometer

The muon spectrometer is designed to detect muons in the polar angular range 2–9° that corresponds to the pseudo-rapidity range $-4.0 \leq \eta \leq -2.5$. The Muon spectrometer of ALICE is composed of five tracking stations, A bending magnetic dipole, a muon shield, and 2 muon trigger stations. Each tracking station is composed of two chambers.

T0

It has the following functions: To generate a timing signal for the Time of Flight (TOF) detector. To measure the vertex position. To provide an early weak up signal to Time Radiation Detector (TRD). To measure the particle multiplicity and generate one of the three possible trigger signals for: minimum-bias, central and semi central events.

Zero Degree Calorimeter (ZDC)

The Zero Degree Calorimeter consist of two neutron (ZNA and ZNC) and proton (ZPA and ZPC) calorimeters located at both sides of ALICE at 116 meters from the interaction point. The main role of ZDC is to estimate the centrality of lead-lead collisions through the observation of the number of participant nucleons. This can be estimated by measuring the energy propagated in the forward direction by the spectator (not participating) nucleons from the collision. The more central the collision, less spectator nucleons in the forward direction. At the location of the ZDC the beam pipe coming from IP 2 is forked in two separated pipes, one carrying bunches to the interaction point and the other transporting bunches from it. This separation is done by the magnetic elements of the LHC, and affects the charged spectators from the collision, separating the neutral hadrons which stay basically on the continuation of the beam line from the charged hadrons which are deflected. This is why the neutron calorimeter lies at zero degree from the beam axis while the ZP is placed externally to the beam pipe on the side where positive particles are deflected.

1.1.4 The Central Trigger Processor (CTP)

At the LHC, bunches consisting of tightly packet protons (approximately 10^{11} per bunch) are injected into the 27 km circular accelerator, reaching velocities very close to speed of light. Each bunch orbits the LHC 11245 times a second. Along the beam, there are special moving positions, called RF buckets, where the bunches can be placed. The RF buckets are separated 2.5 ns or about 75 cm but generally the bunches are separated by 10 RF buckets.

The LHC can be filled with up to 2808 bunches per beam pipe. In this conditions there will be about $2808 \times 11245 = 31.6$ millions of bunch crossings per second. The probability of having a proton-proton collision in a bunch crossing is called μ value and depends on the luminosity at the interaction point. At ALICE luminosities, typical μ values are in the order of 0.1 meaning that we will have an event rate of the order of a few millions per second. Storing the information produced by all the detector at this rate, with current IT technology is a very hard if not impossible challenge. It is therefore necessary to reduce the event rate to manageable levels by filtering out non interesting (or already well known) events.

The role of the CTP, is to receive quick preliminary data about the current event, and then decide if the event should be stored for further offline analysis, or be discarded and lost forever. These decisions are taken in a series of steps or so called trigger levels, namely L0, L1 and L2.

In the first level, just after two bunch of protons cross each other (BC) at the interaction point (IP), the fastest detectors send early preliminary information to the CTP. This are called L0 inputs, and must arrive to the CTP at most 800 ns after the corresponding BC. With these L0 inputs, the CTP makes a first decision (in up to 100 ns) on if it should strobe some detectors and warn them about a potentially interesting event. This L0 decision arrive to detectors at most 1.2 μs after the corresponding BC.

Those detectors that are not fast enough to reach the L0 level, are waited by the CTP up to 6.1 μs (after the corresponding BC) for their L1 inputs. Then, after 6.5 μs from the BC, CTP sends the L1 message to detectors.

Some detectors may have not finish the processing of the current event by the time the next bunch crossing arrives. For example, the TPC needs up to 90 μs. If during this time, another event leaves a large number of tracks in the TPC, it can turn the data unreconstructible. For this reason, the CTP waits up to 105 μs to check if there are overlapping events during this period (past-future protection). Then, it send the L2a (event accepted) or L2r (event rejected) messages, indicating that the event should be stored or discarded, respectively,

After all this steps, the rate of accepted event is in the range of 100 to 1000 Hz, which is manageable by current storage and IT technologies.

1.2 The ALICE Physics Program and observables

ALICE is an LHC experiment devoted to the study of strongly interacting matter in proton-proton, proton–nucleus and nucleus-nucleus collisions at ultra-relativistic energies. It is also well suited the study of high energy diffraction and ultra-peripheral collisions. For these studies ALICE uses the following observables:

Particle multiplicities The average charged-particle multiplicity per rapidity unit (dN_{ch}/dy) is one of the most fundamental observables. In the theoretical side it fixes a global property of the medium in the collision. Since it is related to the attained energy density, it enters in the calculation of most other observables. On the experimental side, the particle multiplicity fixes the main unknown in the detector performance; the charged-particle multiplicity per rapidity unit largely determines the accuracy with which many observables can be measured.

Particle yields and ratios The bulk of particles emitted in heavy-ion collisions are soft hadrons which decouple from the collision in the late hadronic freeze-out of the evolution. They provide information on the freeze-out temperature and chemical potential, radial flow velocity, direct and elliptic flow coefficients, size parameters as extracted from two-particle correlations, event-by-event fluctuations and correlations of hadron momenta and yields. Furthermore, different aspects of the final hadronic momentum distributions are determined at different times of the collision enabling to trace the evolution of the fireball.

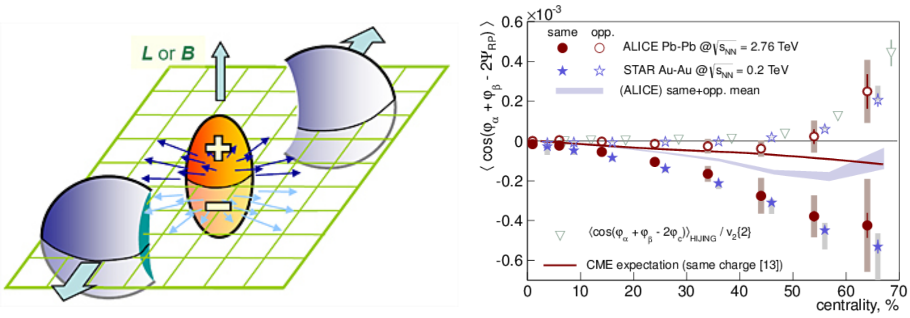

Figure 1.6: Chiral Magnetic Effect (CME) in ALICE. Left: Illustration of the charge separation with respect to the reaction plane induce by the magnetic field created by the heavy-ions. Right: Measurement of charge separation with respect to the reaction plane from the ALICE experiment [25]

1.2.1 Latest Results from ALICE

1.2.2 Chiral Magnetic Effect in QGP

In the early stages after the big-bang, topological charge transitions in the electroweak matter induced nonzero baryon + lepton number which is an evidence of C and CP violation in the universe. In strongly interacting matter produced in heavy-ion collisions induce a difference in the number of left and right handed fermions evincing a P and CP violation in QCD. When two heavy-ion collide strong electromagnetic fields are created in the direction perpendicular to the reaction plane fig. 1.6, defined by the beam axis and the impact parameter.

This magnetic field cause the spin of the quarks to align and in consequence their respective momentum become parallel or anti-parallel to the magnetic field. In the hot dense matter created in the overlapping zone of the collision there will be equal amounts of left and right handed quarks. The right handed quarks will have their spin parallel to their momentum and the left handed quark anti-parallel. Since for a quark specie of a given sign there will be equal amount of right handed particles with momentum parallel and left handed particles with momentum anti-parallel to their spin (and in consequence to the magnetic field), the net amount of charge flowing in this region is zero. Nevertheless topological charge changing transition induces quarks of the same charge to acquire a specific handedness different to quark of opposite charge. This will result in a polarization of the interaction region and a charge separation relative to the reaction plane.

The ALICE experiment using the TPC, SPD, VZERO and ZDC detectors measured (fig. 1.6, right) charge dependent azimuthal correlations in Pb+Pb collision at the center of mass energy per nucleon pair $\sqrt{S_{NN}} = 2.76$ TeV in the pseudorapidity range $|\eta| < 0.8$.

A clear signal compatible with a charge-dependent separation relative to the reaction plane was observed. However, the results are not properly described by the only available quantitative model for the LHC energy.

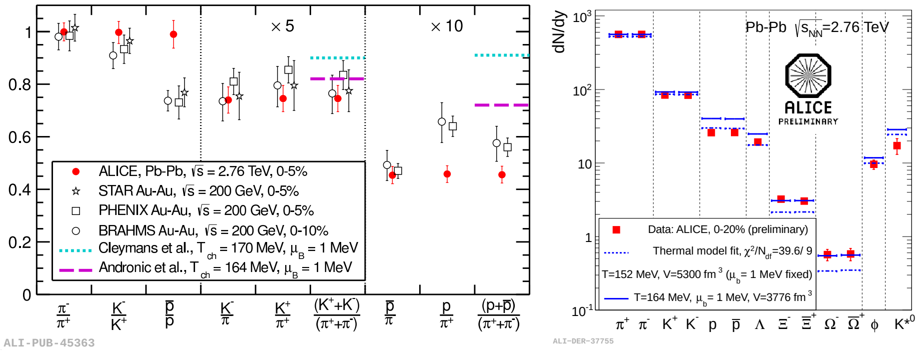

Figure 1.7: Ratios of particle yields measured by the ALICE collaboration in lead lead collisions (right) and preliminary thermal fits to this data. Extracted from [24]

1.2.3 Particle yields

The measurement of transverse momentum distributions (p_T) and yields of identified particles at high energy heavy-ion collisions at the LHC allows the study of thermal and collective properties of nuclear matter under extreme conditions, like the quark gluon plasma predicted by QCD. Hydrodynamic models were found to be in good agreement with results at low energies. In these models the initial hot dense partonic matter rapidly expands and cools down until it experiment a transition to a hadron gas phase. When the observed particle abundances are described in terms of thermal models, the relative abundance in thermal and chemical equilibrium are described mainly by two parameters, the chemical freeze-out temperature, T_{ch} and the baryochemical potential μ_B, where the latter describes the net baryon content of the system. On the other hand particle momentum distributions reflects the conditions at the *kinetic freeze-out* from the hadron-gas phase, when inelastic interactions ends. The p_T distributions encode information about the collective transverse expansion (radial flow) and the temperature at kinetic freeze-out T_{kin}. Using the particle identification capabilities of the TPC and TOF, the ALICE experiment was able to measure the pion, kaon and proton yields at central Pb+Pb collision at $\sqrt{S_{NN}} = 2.76$ TeV and particle ratios (fig. 1.7, left) and, after comparison with several models, best agreement was found with viscous hydrodynamic models with a posterior hadronic cascade transport [24].

It is found that the data is well described by a fit with $T_{kin} = 90 \pm 10$ MeV. The particle ratios for particles and antiparticles are all unity within errors consistent with a vanishing baryochemical potential μ_B. The ratios $K/\pi = (K^+ + K^-)/(\pi^+ + \pi^-)$ and $p/\pi = (p + \bar{p})/(\pi^+ + \pi^-)$ where also measured. The ratios $K/\pi = 0.149 \pm 0.010$ is similar to results at lower energy but the ratio $p/\pi = 0.046 \pm 0.003$ is lower than the expectation from thermal models by a factor of 1.5. Finally a preliminary thermal fit (fig. 1.7, right) of the particle yields founds the chemical freeze-out temperature to be $T_{ch} = 152$ MeV although it was predicted to be $T_{ch} = 164$.

1.2.4 Ultra-Peripheral Collisions

Ultra Peripheral collisions are those in which the impact parameter is greater than the sum of the radii of the two colliding nuclei ($b > R_1 + R_2$). Under this conditions only electromagnetic interactions will occur. The electromagnetic fields produced in this events are characterized for being very intense and of short duration [18]. Fermi and later Weizsäcker and Williams showed that the electromagnetic field of a relativistic particle can be seen as an equivalent flux of photons , being the their number proportional to Z^2 [16].

The produced photons can interact between them or with the nuclei resulting in the production of diverse particles.

Ultra-peripheral collisions can be classified as [18] *exclusive interactions* in which both nuclei are left intact and *inclusive interactions* when any of the nuclei breaks up. In both cases the events are characterized by the presence of one or more rapidity gaps.

It is possible to factorize the total cross section of exclusive and inclusive processes into a photon flux and a photon-photon or photon-nuclei cross section [17] as shown in eq. (1.2.1) and eq. (1.2.2), respectively.

$$\sigma(A + A \to A + A + X) = \int_0^1 \int_0^1 f(x_1) f(x_2) \sigma_{\gamma\gamma}(\hat{s}) dx_1 dx_2 \tag{1.2.1}$$

$$\sigma(A + A \to A + X) = \int_0^1 f(x) \sigma_{\gamma A}(\hat{s}) dx \tag{1.2.2}$$

where $f(x_i)$ is the spectrum of photon energies, with x_1, x_2 the ratios of the photons to projectile energy and $\sigma_{\gamma\gamma}(\hat{s})$ is the two-photon cross section evaluated at $\gamma\gamma$ center of mass energy squared $\hat{s} = x_1 x_2 s$. Analogously fro the inclusive case, $\sigma_{\gamma A}(\hat{s})$ is the photon-nuclei γA cross section at $\hat{s} = xs$. The two-photon interaction can result in the creation of any particle-antiparticle pair like leptons, vectorial bosons or quarks. In the last case the quarks can appear as a bound state (i.e. a resonance) or as two jets coming from the fragmentation of the quarks [17]. The photon induced exclusive interactions are dominated by the exclusive production of vectorial bosons $\gamma A \to VA$.

Exclusive photo production of vector mesons, where a vector meson but no other meson is produced, is of particular interest. Exclusive production of J/Ψ in photon-proton interactions $\gamma p \to \mathrm{J}/\Psi$ has been modeled in terms of perturbative QCD as the exchange of two gluons with no net charge transfer. This together with HERA data allowed the constraint of proton gluon-distribution at low Bjorken-x. Similarly exclusive vector meson production in heavy ion interactions are expected to probe the nuclear gluon-distributions.

Exclusive photoproduction can be coherent, where the photon couples coherently with all the nucleons, or incoherent, where the photon couples with a single nucleon. Coherent production is characterized by low p_T and no breakup of the target nuclei. Incoherent production is characterized by a higher transverse momentum and the breakup of the target nuclei. In this last case, apart from the fragments of the targeted nucleus at high rapidity, no other particles are produced.

At the LHC the ALICE Collaboration has made the first measurement of J/Ψ photoproduction in ultra-peripheral Pb–Pb collisions [26]. The J/Ψ is identified via its decay to two muons in the forward rapidity region with the ALICE muon spectrometer for events where the hadronic activity is required to be minimal. The cross section for coherent J/Ψ production in the rapidity interval $-3.6 < y < -2.6$ is measured to be $d\sigma^{\mathrm{coh}}_{\mathrm{J}/\psi}/dy = 1.00 \pm 0.18(\mathrm{stat})^{+0.24}_{-0.26}(\mathrm{syst})$ mb. The result is compared to theoretical models for coherent J/Ψ production and found to be in good agreement with those models which include nuclear gluon shadowing.

1.2.5 Flow

The term flow refers to the appearance of an overall pattern in the expansion of matter in the collision of heavy nuclei. This arises from the interaction of multiple outgoing particles and affects all or almost all of the particles of the event. It is to note that although the notion of flow does not necessarily imply an hydrodynamic behavior, it is customary to picture the underlying physics in terms of pressure gradients.

The characteristics of this *flow* depend on the energy, and centrality of the collision, and also in the properties of the system at the freeze out. At low energies where relatively few new particles are created, flow effects are mostly caused by nucleons from the incoming nucleus so that their interpretation relies on notions like the compressibility of the nuclear matter or the competition between two-body interactions and mean field effects. At high energies the observable flow effects are dominated by the large number of newly created particles while the primordial nucleons make only a minor contribution. In this last regime the theoretical interpretation is based on microscopic transport (cascade) in which flow depends on the partonic and hadronic cross sections and the thermodynamic approach which can be applied when the mean free path of the particles is much smaller than the system size and allows to use the equation of state and to define a sound speed for the medium.

Isotropic flow If the collision is central then the superposition of the two spherical colliding nuclei will be symmetrical in azimuth and will lead to an isotropic distribution of the particles in the final state. Any pressure gradient will cause an azimuthally symmetric collective flow of particles called *radial* flow. For a particular particle species the random thermal motion will be superimposed on the collective radial flow which will be reflected on the invariant transverse momentum distribution depending on the temperature at freeze-out, particle mass and velocity profile in space-time.

Anisotropic flow In non central heavy-ion collision the overlapping region will introduce an azimuthal asymmetry in configuration space which will translate into an azimuthal asymmetry in the transverse momentum distribution of the outgoing particles called *anisotropic flow.*

At low energies this anisotropic flow is dominated by the pressure build up between the two nuclei with the flow of nucleons having its maximum in the reaction plane determined by the impact parameter and the beam axis. This collective phenomena is called *direct flow.*

In ultra-relativistic heavy-ion collisions most of the particles are produced in the interaction volume and can exhibit additional flow patterns. The momentum tensor of these particles can be visualized in the transverse plane as an ellipse

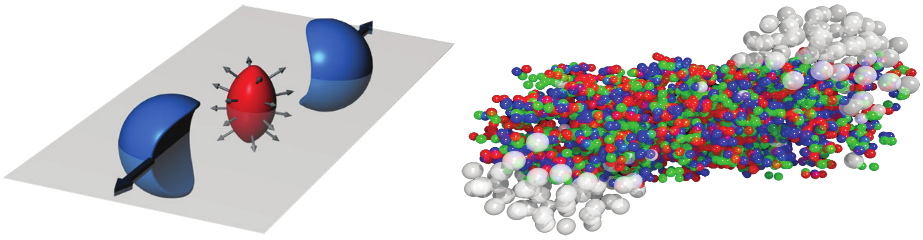

Figure 1.8: Interaction volume in a Lead-Lead collision. From [20]

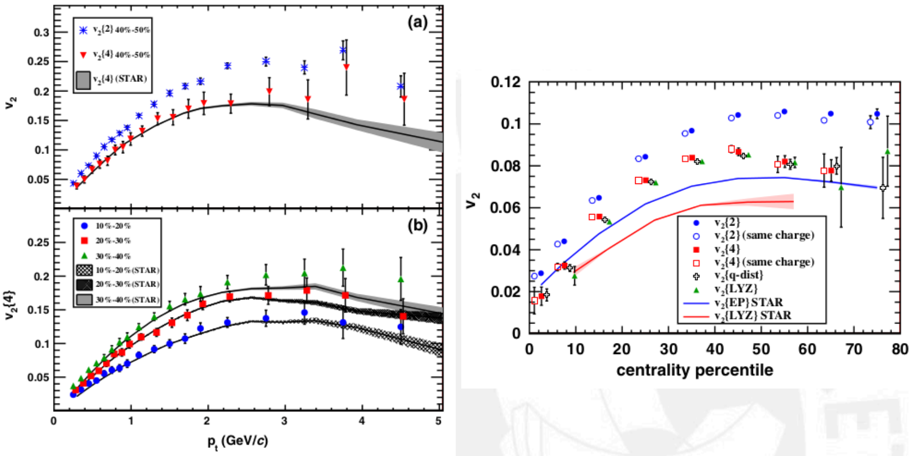

Figure 1.9: Elliptic flow as seen by ALICE. From [21]

with the principal axis either parallel or perpendicular to the reaction plane. The corresponding dominant flow pattern is called *elliptic flow*.

A convenient way of characterizing the various patterns of anisotropic flow is to use a Fourier expansion of the triple differential invariant distribution:

$$E\frac{d^3N}{d3\mathbf{p}} = \frac{1}{2}\pi\frac{d^3N}{p_t dp_t dy}\left\{1 + 2\sum_{n_1}^{\infty}\nu_n(p_t, y)\cos[n(\varphi - \Psi_R)]\right\} \tag{1.2.3}$$

where φ and Ψ_R are the particle and reaction plane azimuths in the laboratory frame respectively. The sine terms in this expansion vanish due to reflection symmetry with respect to the reaction plane. The Fourier components in eq. (1.2.3) are given by

$$\nu_n(p_t, y) = \langle\cos[n(\varphi - \Psi_R)]\rangle \tag{1.2.4}$$

where the angular brackets denote an average over the particles in the (p_t, y) bin under study. With this parametrization, the elliptic flow is defined as the second moment of the azimuthal distribution of produced hadrons (ν_2).

The ALICE experiment made the first measurement of elliptic flow at the LHC [21] at $\sqrt{S_{NN}} = 2.76$ TeV in the central pseudorapidity region ($|\eta| < 0.8$) and transverse momentum range $0.2 < p_t < 5.0$ GeV/c finding it to be in agreement with some hydrodynamic models suggesting the presence of viscosity in the medium at the early times of the collision.

Chapter 2

Physics of High Energy Diffraction

2.1 History of Regge Theory

In 1935 the Japanese physicist Hideki Yukawa hypothesized that particles of about 100 MeV should be responsible for the strong nuclear interaction. In 1947 these mesons revealed themselves in photographic plates exposed to cosmic rays at hight altitude. Among them was the long anticipated pion. Soon it become clear that although this particle plays a role in mediating the strong force, it could not be the only responsible. Rather one has to include the contributions from other mesons in a way that is prescribed by the Regge formalism.

Regge theory can be seen as an extension of the solutions to the problem of symmetrically spherical potentials in non-relativistic quantum mechanics. These solutions are bound states characterized by a positive integer angular momentum and are the poles of the partial wave amplitude $a_\ell(k)$ (where ℓ denotes the angular momentum and k the wave number).

In 1959, Tullio Regge let the orbital angular momentum to take continuous values in the complex plane such that:

$$a(\ell, t) = a_\ell(k) \tag{2.1.1}$$

where one recover the $a_\ell(k)$ for integer values of ℓ.

Regge found that when the potential of the Schrödinger equation takes the form of a superposition of Yukawa potentials the $a(\ell, k)$ exhibit singularities that are single poles. This poles lie in trajectories in the complex plane described by:

$$\ell = \alpha(k) \tag{2.1.2}$$

Chew and Gribov originally extended this treatment to relativistic scattering theory. Here the relativistic scattering amplitude $A_\ell(t)$ is analytically continued to complex ℓ values in a unique way, the resulting function has poles at:

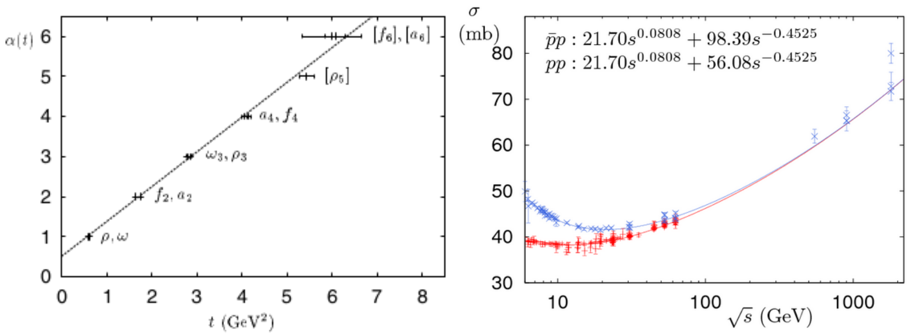

Figure 2.1: Left: Leading Regge trajectories. Right: Total cross section for proton-proton (dashed line) and proton-antiproton (solid line)

$$\ell = \alpha(t) \tag{2.1.3}$$

These poles are known as Regge poles, or reggeons. What is interesting about this trajectories, is that when $t = m^2$ then $\alpha(t = m^2)$ takes integer values corresponding to the spin of the particle with squared mass m^2 in the Regge trajectory. Thus, Regge trajectories describe a family of particles whose combined exchange must be considered together for the calculus of the cross section.

For low t values this trajectories can be approximated as:

$$\alpha(t) = \alpha(0) + \alpha' t \tag{2.1.4}$$

where $\alpha(0)$ is called the intercept and α' the slope of the trajectory.

According to the Regge theory, the contribution of each pole to the total proton-proton scattering amplitude is given by a term which behaves asymptotically ($s \to \infty$ and t fixed) as

$$A(s,t)_{s\to\infty} \sim s^{\alpha(t)} \tag{2.1.5}$$

And contributes to the total cross section:

$$\sigma_{s\to\infty} \sim \frac{1}{s}\mathrm{Im}A(s,t=0)_{s\to\infty} \sim s^{\alpha(0)-1} \tag{2.1.6}$$

This last equation give us a very interesting information: if the intercept is lower than one, the contribution of a trajectory to σ is decreasing with the energy $\sqrt{s}$.

It turns out that all known mesons have intercepts that are smaller than unity (fig. 2.1). This leads to the expectation that the total cross section for hadron scattering should decrease with energy.

Although initially experiments seemed to confirm that behavior at low energies it was soon found that at higher energies the total cross sections begin to level and seemed to be constant around $\sqrt{s} = 20$ GeV.

The explanation to this on terms of Regge theory was the existence of a trajectory with an intercept $\alpha(0) = 1$. This trajectory was named the **pomeron** after the Ukrainian Soviet physicist Isaak Pomeranchuk, who show that the total cross section of proton-proton and antiproton-proton scattering should be asymptotically equal at high energies.

Later with higher energies available it was clear that the total cross section rises with energy, and the Pomeron intercept was fitted to $\alpha_P = 1.08$

2.2 The Pomeron in QCD

In Regge theory, the pomeron is a trajectory with vacuum quantum numbers and α_P= 1 used to explain the constancy of the cross section with energy.

One of the earliest model was proposed by Landshoff and Polkinghorne in the 70's. In this model the pomeron interacts with the quark like a $C = +1$ photon as show in fig. 2.2 (left) and the quark-quark scattering amplitude is given by:

$$-g^2\left[\frac{1+e^{-i\pi\alpha_P(t)}}{\sin\pi\alpha_P(t)}\left(\frac{s}{s_0}\right)^{\alpha_P(t)-1}\right](\bar{u}\gamma^\mu u)(\bar{u}\gamma_\mu u) \tag{2.2.1}$$

where g is the pomeron-quark coupling, u the quark spinor and the quantity in square brackets is the pomeron propagator. Using this amplitude the proton-proton elastic cross section is found to be:

$$\frac{d\sigma_{\text{el}}}{dt} = \frac{g^4|3F_1(t)|^4}{4\pi\sin^2\left(\frac{\pi\alpha_P(t)}{2}\right)}\left(\frac{s}{s_0}\right)^{2\alpha_P(t)-2} \tag{2.2.2}$$

where $F_1(t)$ is the charge form factor of the proton. Donnachie and Landshoff fitted this equation to the data obtaining:

$$\alpha_P(0) = 1.08\alpha_P(0)' \qquad = 0.25\text{GeV}^{-2}g^4 = 3.21\text{GeV}^{-2} \tag{2.2.3}$$

values that were confirmed by further measurements.

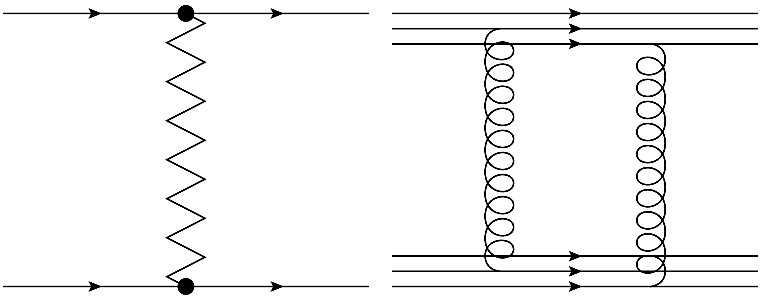

Figure 2.2: Left: Photon-like pomeron before QCD. Right: Pomeron as a two gluon exchange

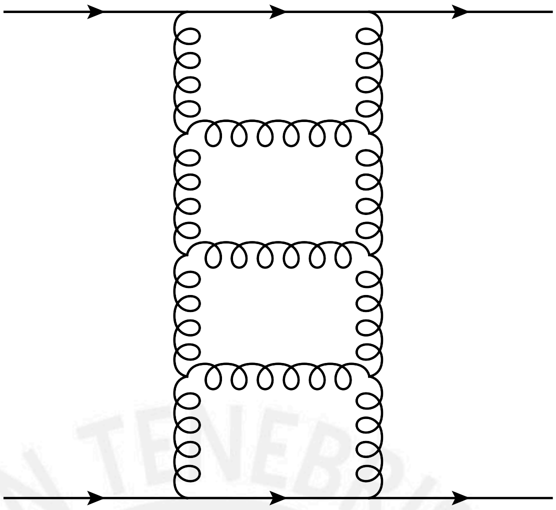

Figure 2.3: The BFKL pomeron as a gluon ladder

Later, Low and Nussinov make an attempt to explain the nature of the pomeron in terms of QCD fundamental constituents by proposing a model in which the pomeron is viewed as a *two-gluon exchange*, which is the minimum number of gluons able to produce a colorless combination.

In general the two gluons could couple either to the same quark or different quarks in the colliding hadrons. The latter case is incompatible with the photon like interaction between quarks and pomeron proposed by Standoffish. However, if the gluon correlation length in the QCD vacuum is much smaller than the hadron radius, the diagrams where the gluon couple to different quarks are strongly suppressed. In this way non-perturbative effects establish a bridge between the two models.

In perturbative QCD, on the other hand, using the Balitsky Fadin Kuraev Lipatov (BFKL) equation the pomeron can be pictured as an exchange of gluon ladders as shown in fig. 2.3. This leads to a hard pomeron with intercept $\alpha_P^{\text{hard}} \simeq 1.5$ for $\alpha_s = 0.2$.

2.3 Diffraction

In a general way, diffraction can be defined in the following terms:

A reaction in which no quantum numbers are exchanged between the colliding particles is, at high energies, a diffractive reaction

This definition is simple and general enough to cover all cases:

I *elastic scattering* when exactly the same incident particles come out after the collision.

$$1 + 2 \to 1' + 2'$$

II *single diffraction* when one of the incident particles is intact after the collision while the other gives rise to a bunch of final particles (or to a resonance) with the same quantum numbers.

$$1 + 2 \rightarrow 1' + X_2$$

III *double diffraction* when each incident particle gives rise to a bunch of final particles (or resonance) with the same quantum numbers of the two initial particles

$$1 + 2 \rightarrow X_1 + X_2$$

IV *central diffraction* when the same incident particles came out after the collision but a central system is created that gives rise to a bunch of particles (or resonance) with the quantum numbers of the vacuum.

$$1 + 2 \rightarrow 1' + X + 2'$$

In the practice, however, it can be difficult to prove that the only exchanged quantum numbers were those of the vacuum if the final states were not completely reconstructed.

Then it is convenient to give an operational definition of diffraction as follows: *A diffractive reaction is characterized by a large non-exponentially suppressed rapidity gap in the final state*

Rapidity gaps can also occur in non-diffractive events due to multiplicity fluctuations but the number of these event are exponentially suppressed. If we denote by $\Delta\eta$ the rapidity gap of the final state, the distribution of diffractive events is

$$\frac{dN}{d\Delta\eta} \sim \text{constant} \tag{2.3.1}$$

While for non-diffractive events is

$$\frac{dN}{d\Delta\eta} \sim e^{-\Delta\eta} \tag{2.3.2}$$

2.4 Kinematics of diffraction

In the following we review briefly the kinematics of diffraction scattering and the production of rapidity gaps. Lets first define some quantities:

2.4.1 Important physical quantities

The rapidity of a particle with momentum $\boldsymbol{p} = (p_x, p_y, p_z)$ and energy E is defined as:

$$y = \frac{1}{2} \ln \left[\frac{E + p_z}{E - p_z} \right] \tag{2.4.1}$$

and its pseudorapidity is given by:

$$\eta = \frac{1}{2} \ln \left(\frac{|\boldsymbol{p}| + p_z}{|\boldsymbol{p}| - p_z} \right) \tag{2.4.2}$$

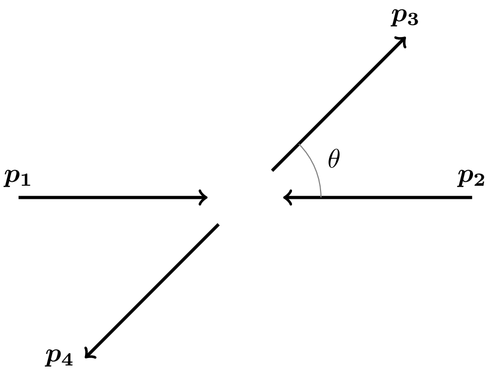

Figure 2.4: Scattering process in the center of mass system

or equivalently

$$\eta = -\ln[\tan(\theta/2)] \tag{2.4.3}$$

where θ is the angle between the initial ($\boldsymbol{p_1}$) and final ($\boldsymbol{p_3}$) momentum of the elastically scattered particle (fig. 2.4).

We define the transverse mass and energy of a particle as:

$$m_\perp = \sqrt{m^2 + p_\perp^2} \tag{2.4.4}$$

$$E = \sqrt{m_\perp^2 + p_z^2} \tag{2.4.5}$$

Lets consider a two body exclusive scattering:

$$1 + 2 \rightarrow 3 + 4 \tag{2.4.6}$$

The Mandelstam variables are:

$$s = (p_1 + p_2)^2 = (p_3 + p_4)^2 \tag{2.4.7a}$$

$$t = (p_1 - p_3)^2 = (p_2 - p_4)^2 \tag{2.4.7b}$$

$$u = (p_1 - p_4)^2 = (p_2 - p_3)^2 \tag{2.4.7c}$$

they follow the relationship:

$$s + t + u = \sum_{i=1}^{4} m_i^2 \tag{2.4.8}$$

which implies that only 2 of them are linearly independent.

Lets remember briefly that:

$$\begin{aligned} s &= (p_1 + p_2)^2 \\ s &= p_1^2 + p_2^2 + 2p_1p_2 \\ s &= m_1^2 + m_2^2 + 2E_1E_2 - 2\boldsymbol{p_1}\boldsymbol{p_2} \end{aligned}$$

but in the C.M. system $\boldsymbol{p}_1 = -\boldsymbol{p}_2$ so:

$$\begin{aligned}
s &= m_1^2 + m_2^2 + 2E_1E_2 + 2\boldsymbol{p}_1\boldsymbol{p}_1 \\
s &= m_1^2 + m_2^2 + 2E_1E_2 + \boldsymbol{p}_1^2 + \boldsymbol{p}_2^2 \\
s &= m_1^2 + \boldsymbol{p}_1^2 + m_2^2 + \boldsymbol{p}_2^2 + 2E_1E_2 \\
s &= E_1^2 + E_2^2 + 2E_1E_2 = (E_1 + E_2)^2
\end{aligned}$$

And since the total energy of the system is $E = E_1 + E_2$, we have, in the center of mass system (CMS):

$$E_{\text{CMS}} = \sqrt{s} \tag{2.4.9}$$

2.4.2 Diffractive scattering and rapidity gaps

Lets now consider the scattering process:

$$1 + 2 = 3 + X$$

referring to the collision of two particles of mass m (1 and 2), one of them experiencing elastic scattering (3), and the other becoming an excited state system of mass M_X which then fragments into a cascade of particles represented by X.

In the center of mass system we have,

$$\begin{aligned}
p_1 &= (E_1, \boldsymbol{p}) \\
p_2 &= (E_2, -\boldsymbol{p}) \\
p_3 &= (E_3, \boldsymbol{p'})
\end{aligned}$$

then, from momentum conservation,

$$\begin{aligned}
(p_1 + p_2)^2 &= (p_3 + p_X)^2 \\
s &= (p_3 + p_X)^2 \\
&= p_3^2 + p_X^2 + 2p_3p_X \\
&= m^2 + M_X^2 + 2E_3E_X - 2\boldsymbol{p_3}\boldsymbol{p_X}
\end{aligned}$$

but again $\boldsymbol{p}_3 + \boldsymbol{p}_X = 0$ and $E = E_1 + E_2 = E_3 + E_4 = \sqrt{s}$, so:

$$\begin{aligned}
s &= m^2 + M_X^2 + 2E_3E_X + 2\boldsymbol{p}_X^2 \\
&= m^2 + M_X^2 + 2E_3E_X + 2(E_X^2 - M_X^2) \\
&= m^2 - M_X^2 + 2E_X(E_3 + E_X) \\
&= m^2 - M_X^2 + 2E_X(\sqrt{s}) \\
\Rightarrow E_X &= \frac{s - m^2 + M_X^2}{2\sqrt{s}}
\end{aligned} \tag{2.4.10}$$

From here is easy to see, using $E_3 = \sqrt{s} - E_X$, that:

$$E_3 = \frac{s + m^2 - M_X^2}{2\sqrt{s}} \tag{2.4.11}$$

In the limit when $s, M_X^2 \gg m^2$:

$$E_X \simeq \frac{s + M_X^2}{2\sqrt{s}} \tag{2.4.12}$$

$$E_3 \simeq \frac{s - M_X^2}{2\sqrt{s}} \tag{2.4.13}$$

Under this approximation, and squaring eq. (2.4.12), we find the momentum $|\boldsymbol{p'}|$

$$\begin{aligned}
E_X^2 = M_X^2 + \boldsymbol{p}_X^2 &= \frac{s^2 + 2s^2 M_X^2 + M_X^4}{4s} \\
4s\boldsymbol{p}_X^2 &= s^2 - 2s^2 M_X^2 + M_X^4 \\
\boldsymbol{p}_X^2 &= \frac{(s - M_X^2)^2}{4s} \\
|\boldsymbol{p}_X| = |\boldsymbol{p'}| &= \frac{(s - M_X^2)}{2\sqrt{s}} \qquad (2.4.14)
\end{aligned}$$

For a very fast particle with momentum $\boldsymbol{p}$ ($p_z \to \infty$) and energy E its rapidity is:

$$y = \frac{1}{2} \ln \left(\frac{E + p_z}{E - p_z} \right)$$

Multiplying by $(E + p_z)/(E + p_z)$ and operating:

$$\begin{aligned}
y &= \frac{1}{2} \ln \left(\frac{(E + p_z)(E + p_z)}{(E - p_z)(E + p_z)} \right) \\
&= \frac{1}{2} \ln \left(\frac{E^2 + 2Ep_z + p_z^2}{E^2 - p_z^2} \right) \\
&= \frac{1}{2} \ln \left(\frac{m_\perp^2 + 2Ep_z + 2p_z^2}{m_\perp^2} \right) \\
&= \frac{1}{2} \ln \left(1 + \frac{2p_z(E + p_z)}{m_\perp^2} \right)
\end{aligned}$$

Since $p_z \to \infty \quad \Rightarrow \quad p_z \gg m \quad \wedge \quad E \simeq p_z$, then

$$\begin{aligned}
y &\simeq \frac{1}{2} \ln \left(1 + \frac{4p_z^2}{m_\perp^2} \right) \\
&\simeq \frac{1}{2} \ln \left(\frac{4p_z^2}{m_\perp^2} \right) \\
&= \ln \left(\frac{2p_z}{m_\perp} \right) \qquad (2.4.15)
\end{aligned}$$

Using eq. (2.4.15) for the scattered particle in the diffractive process (with energy E_3 and momentum $\boldsymbol{p'}$):

$$y = \frac{1}{2} \ln \left(\frac{E_3 + p'_z}{E_3 - p'_z} \right) \simeq \ln \left(\frac{2p'_z}{m_\perp} \right) \tag{2.4.16}$$

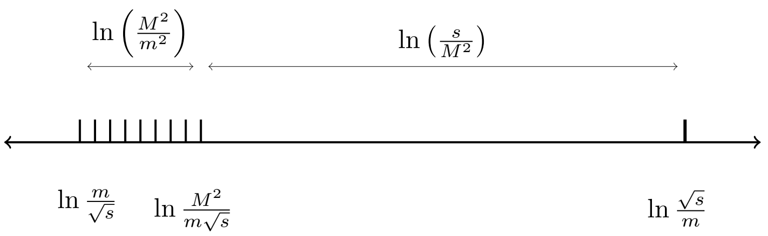

Figure 2.5: Rapidity gap in the single diffractive process $1+2\rightarrow 3+X$

At large $\sqrt{s}$, considering particle 3 as the result of the scattering of 1, and $p'_z > 0$,

$$\begin{aligned} y &\simeq \ln\left(\frac{2}{m_\perp}\left(\frac{s-M_X^2}{2\sqrt{s}}\right)\right) \\ &\simeq \ln\left(\frac{\sqrt{s}}{m_\perp}-\frac{M_X^2}{m_\perp\sqrt{s}}\right) \\ &\simeq \ln\left(\frac{\sqrt{s}}{m_\perp}\right) \end{aligned} \tag{2.4.17}$$

The maximum rapidity y attainable for particle 3 is reached when $p_\perp = 0$:

$$y_{\text{max}} \simeq \ln\left(\frac{\sqrt{s}}{m}\right) \tag{2.4.18}$$

For the diffracted system of mass M_X by the previous discussion we may expect that if we have all the mass M_X concentrated in just one particle its rapidity will be be

$$\langle y_{M_X}\rangle = \ln(\sqrt{s}/M_X) \tag{2.4.19}$$

Due to its compositeness, there will be a distribution in rapidity for the particles originating from this system, the maximum (in absolute value) occurring for a particle of transverse mass $\sim m$ and momentum $\sim \sqrt{s}/2$

$$|y_X|_{\text{max}} \simeq \ln\left(\frac{\sqrt{s}}{m}\right) \tag{2.4.20}$$

whereas the minimum value of $|y_X|$ pertains to a particle with momentum $\sim (m/M)\sqrt{2}$ and transverse mass $\sim M$,

$$|y_X|_{\text{min}} \simeq \ln\left(\frac{m\sqrt{s}}{M^2}\right) \tag{2.4.21}$$

Then the rapidity gap between particle 3 and the edge of the rapidity distribution of the system X is roughly given by

$$\Delta y \simeq \ln\left(\frac{\sqrt{s}}{m}\right) + \ln\left(\frac{m\sqrt{s}}{M^2}\right) = \ln\left(\frac{s}{M^2}\right) \tag{2.4.22}$$

Chapter 3

The AD detector system

3.1 Introduction

As mentioned in the previous chapter, diffractive events can be tagged using pseudorapidity gaps. In order to design effective triggers that can select those events it is important to know their general properties, among them the pseudorapidity distribution of these class of events. For this we will use two Monte Carlo generators, Pythia6[19] and Phojet[8], that implement different models of diffraction and can be used to estimate these distributions.

Before continuing, some conventions will be introduced. The frame of reference for the ALICE experiment is as follows: the positive y axis coincide with the upward direction. The positive x axis is parallel to the horizontal plane and points towards the LHC center. The positive z axis is also parallel to the horizontal plane and its direction is such as to form right handed coordinate system. The origin of coordinates is located at the nominal interaction point. The plane $z = 0$ divides the experiment in two sides, left or C side ($z < 0$) and right or A side ($z > 0$). The ALICE convention dictates that the letters A or C are appended to the name of sub-detectors to denote their location.

In single diffraction events, any of the two colliding protons can break up, while the other remains intact. In what follows we designate as single-diffractive-left (SD-L) events, those in which the proton that breaks up goes to the direction of the negative z axis (i.e has momentum $p_z < 0$) or to the left side. Accordingly, events in which the proton that breaks up goes to the right side ($p_z > 0$) are denoted single-diffractive-right (SD-R).

Single diffraction events have a characteristic particle distribution. Let us consider the case for SD-L. The charged particle distribution $dN_{ch}/d\eta$ has a notorious peak at forward pseudorapidities at $\eta \approx -5$, corresponding to the fragmented proton, and a smaller peak at $\eta \approx -10$ due to the surviving (non-diffracted) proton (fig. 3.1, top). A symmetrical distribution can be found if we exchange the direction between the diffracted and the non-diffracted proton. Double diffraction (DD) happens when both protons become excited and undergo break up. These events present two symmetric peaks at forward rapidities and a dip around $\eta = 0$ (fig. 3.1, bottom left). In central diffraction (fig. 3.1, bottom middle) both protons survive (small peaks at $\eta \approx \pm 10$) but they create a diffracted mass which involves various particles at central rapidities (central peak at $\eta = 0$). The non-diffractive events (ND) do not exhibit pseudorapidity gaps (fig. 3.1, bottom right).

As it has been seen in the previous chapter the individual characteristics of single diffractive events are determined by the energy of the collision and the diffracted mass (M_X). In particular for high masses the gap size is approximately $\Delta\eta \approx \Delta y \approx \ln(s/M_X^2)$. The collision energy $\sqrt{s}$ is fixed by the experiment while the diffracted mass follows an exponential distribution of the form $1/M_X^{f(\Delta)}$. Here $\Delta = \alpha_P - 1$ with α_P the intercept of the pomeron trajectory. The exact form of f depends on the Regge trajectories considered in the Feynman diagram. The uncertainty in the knowledge of this distributions constitute the main contribution to the systematic error in diffractive physics. In fig. 3.2 the probability of having an SD-L event, according to Pythia and Phojet, as a function of the mass of the diffracted system (M_X), is plotted.

It has been observed at the Tevatron ($\sqrt{s} = 1.8$ TeV) that the contribution of diffractive processes represent about 25% of the total inelastic cross section[2] for proton-antiproton. From the previous chapter we know that the cross section of diffractive processes grows as $\ln(s)$, thus, it is expected that the diffractive processes, at the LHC energies, contribute significantly to the total inelastic cross section. In this way, our accurate knowledge of the size of the contribution of the diffractive processes in the inelastic sample, is critical for measuring, with very good precision, the different LHC observables.

In figure 3.1 we observe that the ALICE detectors mostly cover the central pseudorapidity range, for instance, the both layers of SPD are within $|\eta| < 2.0$ and the TPC is in the range of $|\eta| < 0.9$. This coverage is complemented by the FMD and VZERO detectors which extend the ALICE pseudorapidity range to $-3.7 < \eta < 5.1$. Using the SPD, FMD and VZERO we are able to select about 30% of single diffractive events from an inelastic sample.

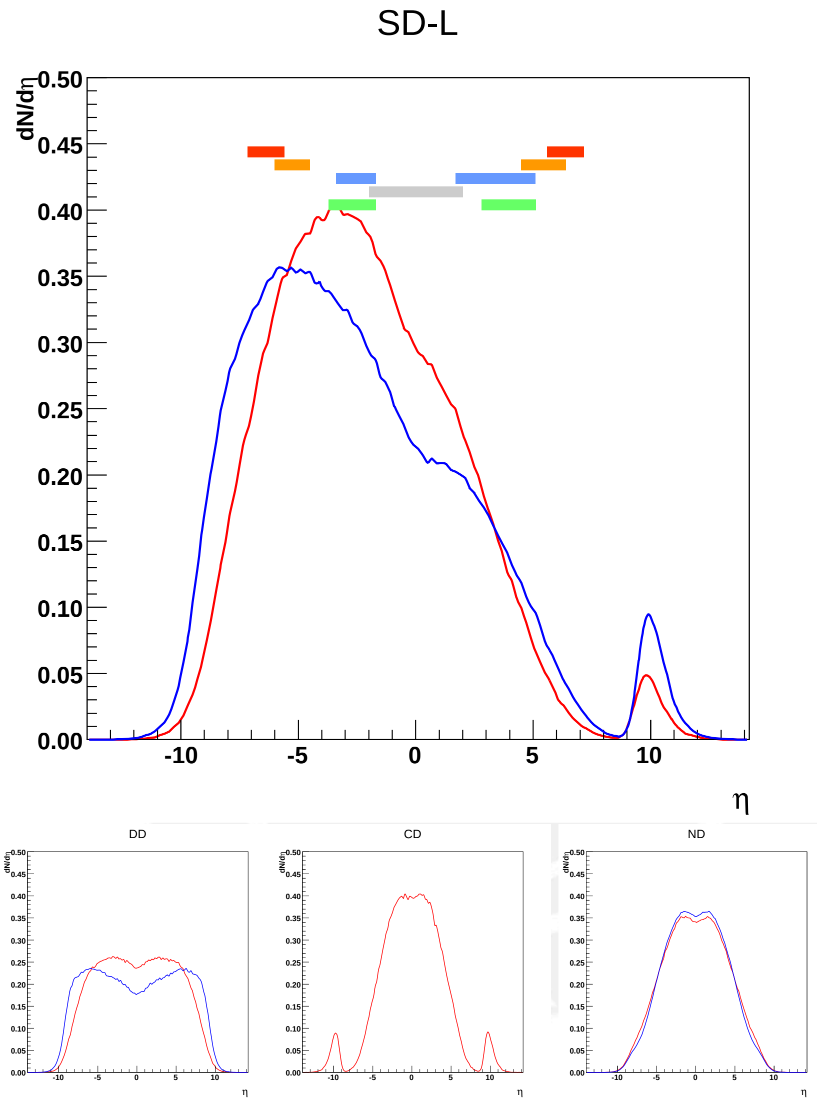

Figure 3.1: Pseudorapidity distribution of primary charged particles for different inelastic processes according to Pythia6 (blue) and Phojet (red). Top: SD-L. Bottom left: Double diffractive. Bottom center: central diffraction. Bottom right: non-diffractive. The colored boxes show the pseudorapidity coverage of SPD (gray), VZERO (green), FMD (light blue), ADC and ADA (yellow), and ADC2 and ADA2 (orange)

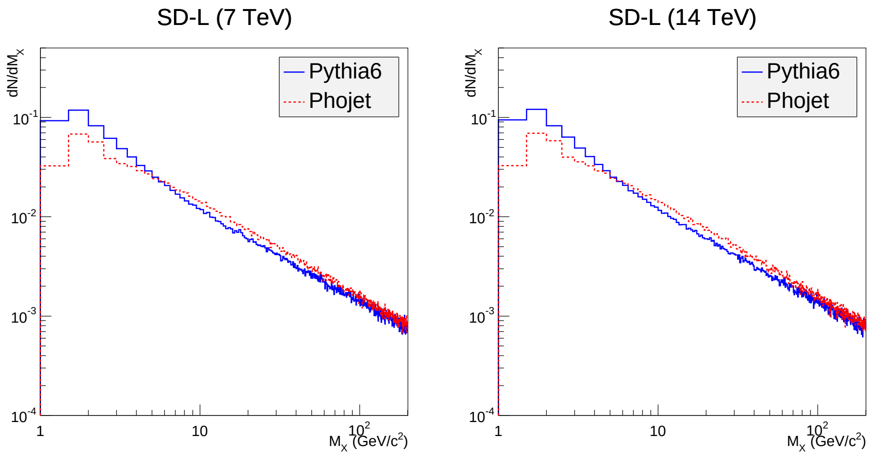

Figure 3.2: Diffractive mass distribution for SD-L events at $\sqrt{s} = 7.0$ (left) and $\sqrt{s} = 14.0$ TeV (right) according to Pythia6 (blue) and Phojet (red).

3.2 AD detector system

The ALICE Diffractive detector (AD) will improve the selection of diffractive events by adding new scintillator stations located at forward pseudorapidities. Four scintillator stations are considered and three possible sets of locations and geometry configuration are studied. These are detailed in the next section.

We show that the selection efficiency for events with diffracted mass below 10 GeV/c^2 (the current ALICE limit) is greatly improved and, as a consequence, the systematic uncertainty in the mean trigger efficiency is reduced, which lead to a reduction in the systematic uncertainty for future measurements of the diffractive cross section in ALICE.

The geometry of the four AD stations was implemented in AliRoot, the official software framework of the ALICE Collaboration. It handles all aspects of simulation and data analysis. In particular a complete description of the geometry and materials of the ALICE experiment components is implemented in its source code. Generation and simulation of events is handled via interfaces to MC generators such as Pythia and Phojet. The transport of particles through the geometry and materials of the ALICE experiment is handled via interfaces to Geant3. The deposition of energy in the sensitive elements of detectors is stored in specific hits classes for each detector. The conversion of hits to simulated electronic response, without noise, of detector is stored in summable digits (SDigits). After the addition of noise they are converted into Digits, representing the final simulated electronic signal from the detector.

The procedure for including the code of the new detector into AliRoot was to modify the source code of the ZDC detector. This was done since it was foreseen that the detectors would be readout using ZDC electronics. The simulations done in this work include the generation of events with Pythia6 and Phojet, the transport of the particles through the full ALICE geometry and the analysis of the hits generated by the passage of particles.

For the simulation of events the Legion super computing system at PUCP was used, implemented by the DIA using BOINC open source framework, Linux virtual machines with our modified version of AliRoot including the AD stations geometry, and grid computing techniques to profit from the computer power of approximately 250 cores distributed along the university campus. This allows us to generate millions of events in the term of days that otherwise could take years on a single computer.

The naming convention for these stations is as follows. On the A side ($z > 0$), the station closest to the interaction point is called ADA1 and the farthest ADA2. Similarly on the C side ($z < 0$) the closest station to the interaction point is called ADC1 and the farthest ADC2

3.3 The Geometry of the detectors

The material used in the simulation of these detectors is a plastic polymer with base of polyvinyl-toluene, having a density of 1.032 g/cm^3, and containing 5.23×10^{22} and 4.74×10^{22} atoms of hydrogen and carbon per cm^3, respectively.

setup	parameter	ADA	ADC	ADA2	ADC2
I	z (m)	7.77	−19.50	55.00	−55.00
	$\eta_{\rm min}$	3.78	−5.97	6.53	−7.52
	$\eta_{\rm max}$	5.65	−4.52	7.52	−6.53
	$R_{\rm min}$ (cm)	–	–	6.0	6.0
	$R_{\rm max}$ (cm)	–	–	16.0	16.0
II	z (m)	7.77	−19.50	22.50	−22.50
	$\eta_{\rm min}$	3.78	−5.97	5.64	−7.16
	$\eta_{\rm max}$	5.65	−4.52	7.16	−5.64
	$R_{\rm min}$ (cm)	–	–	6.0	6.0
	$R_{\rm max}$ (cm)	–	–	16.0	16.0
III	z (m)	17.00	−19.50	22.50	−22.50
	$\eta_{\rm min}$	4.57	−5.97	5.64	−7.16
	$\eta_{\rm max}$	6.43	−4.52	7.16	−5.64
	$R_{\rm min}$ (cm)	–	–	3.5	3.5
	$R_{\rm max}$ (cm)	–	–	16.0	16.0

Table 3.1: The different configurations of the AD stations simulated in this work

In table 3.1 we show a summary of the different configurations of the AD stations tested in this work. Below we describe the geometry of the AD stations in each configuration.

3.3.1 ADC1

It is a square shaped scintillator 60 cm side and 4 cm thick. It features a hole in the form of a rotated H letter as shown in fig. 3.3 in order to make room for the beam pipe and screws found at the place of installation. It was physically installed at $z = -19.50$ meters from the interaction point. The radius of the inscribed circle to the hole is 10 cm. The radius of the circumscribed circle to the detector is 42.42 cm. It is divided into four sectors (referred in the simulation code with numbers from 1 to 4).

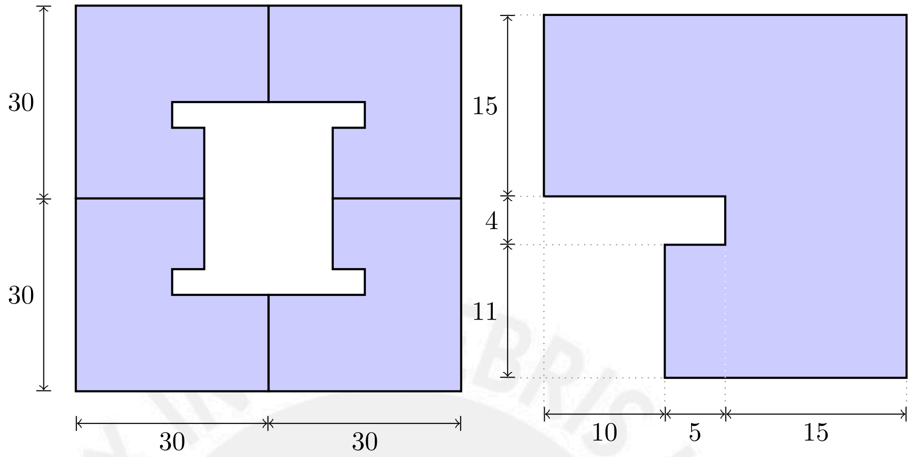

Figure 3.3: Left: Schematic view of the ADC1 detector. Right: detail of one sector. All lengths are in units of centimeters.

3.3.2 ADA1

It is a squared scintillator 50 cm side and 4 cm thick (fig. 3.4) with a rhomb shaped hole at the center in order to make room for the beam pipe. This rhomb is 10 cm side. It was physically installed at $z \simeq 777$ cm and was operated as a beam loss monitor from DCS. In this work the ADA was simulated at its actual location and at $z = 1950$ cm finding a big improvement in performance at the last one.

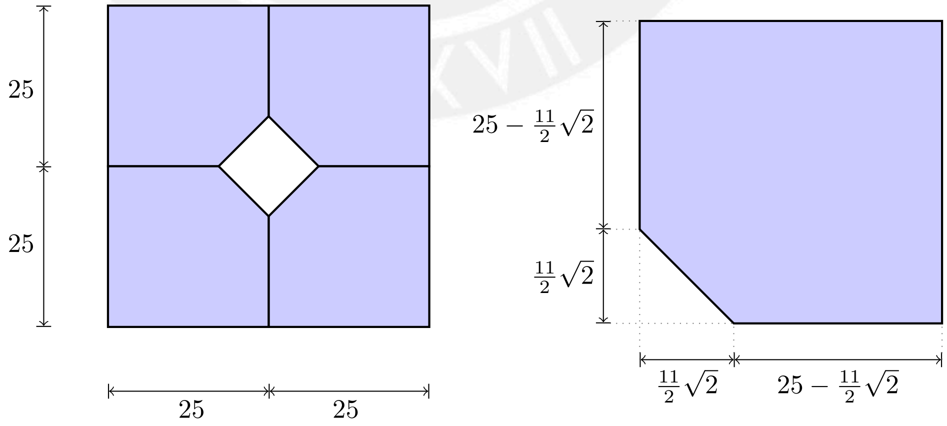

Figure 3.4: Left: Schematic view of the ADA1 detector. Right: detail of one sector.

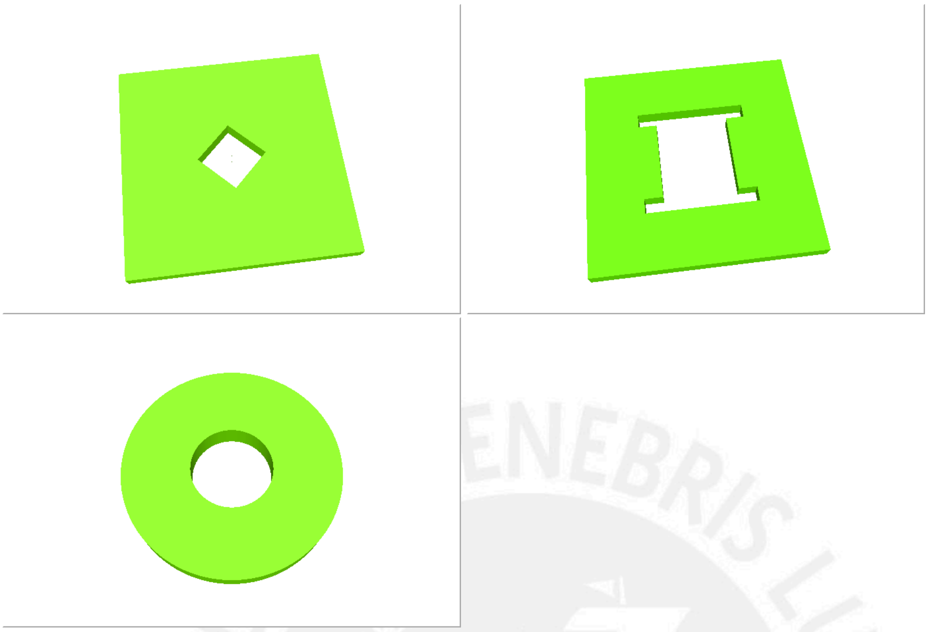

Figure 3.5: The AD detector system. Top left: ADA. Top right: ADC. Bottom: ADC2 and ADA2.

3.3.3 ADA2 and ADC2

The ADC2 and ADA2 detectors are two planned scintillator rings designed to increase the rapidity coverage of the AD stations. It was initially thought to locate this stations at $z \pm 55$ meters with an inner radius $R_{in} = 6$ cm and outer radius of $R_{out} = 16$ cm (fig. 3.6: left). Nevertheless, simulations done in this work showed that the efficiency per event would be very low at these locations, due to the presence of several LHC magnetic elements. They were repositioned in the simulation to $z = \pm 22.5$ meters from the interaction point and their inner radius reduced to $z = 3.5$ cm (fig. 3.6: right)in order retain some of the gain in the rapidity coverage. This small radius was compatible with the beam pipe at the simulation level. Here we assume that the geometry description of the beam pipe in AliRoot is correct in that sense. The detectors have a thickness of 4 cm and are divided in four sectors each (this sectors are referred in the simulation internals via the `SQ` number, 9 to 11 for the ADC2 and 13 to 16 for the ADA2).

Although the location and shape of this station were chosen to have a high efficiency for diffractive events there were several space and material budget constraints which limited the options for optimal positions. The beginning of the Long Shutdown on 2013 opens the possibility to modify several material elements like shielding and perhaps increase even further the performance of these AD stations.

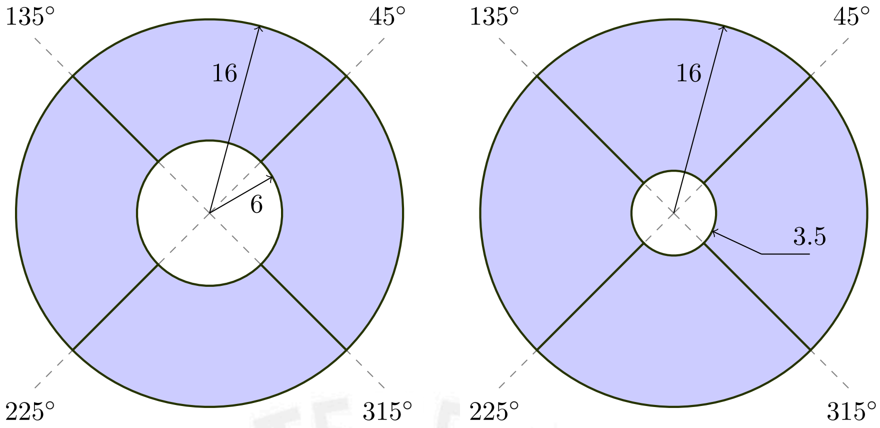

Figure 3.6: Schematic view of the two configurations for the circular AD stations. Left: geometry at $z = \pm 55$ meters. Right: at $z = \pm 22.5$ meters. All lengths are in units of centimeters.

3.3.4 Performance

Average hit density per event

In fig. 3.7 we show the average charged hit density on the AD scintillators for single diffractive events. Here we did separate simulations for the case when the diffracted mass goes to the C-Side (SD-L) and when it goes to the A-side (SD-R) of ALICE. As expected, the average charged hit density is higher when the products of the diffracted system fly in the direction of the detector and lower in opposite case.

The major fraction of hits in the detectors are due to secondary tracks created from the interaction of primary particles with structures such as the beam pipe and shielding blocks. We give more details about the origin of secondaries in the next section.

Note that zones of higher density in the detectors are located near the beam pipe, which is a structure with high production of secondaries.

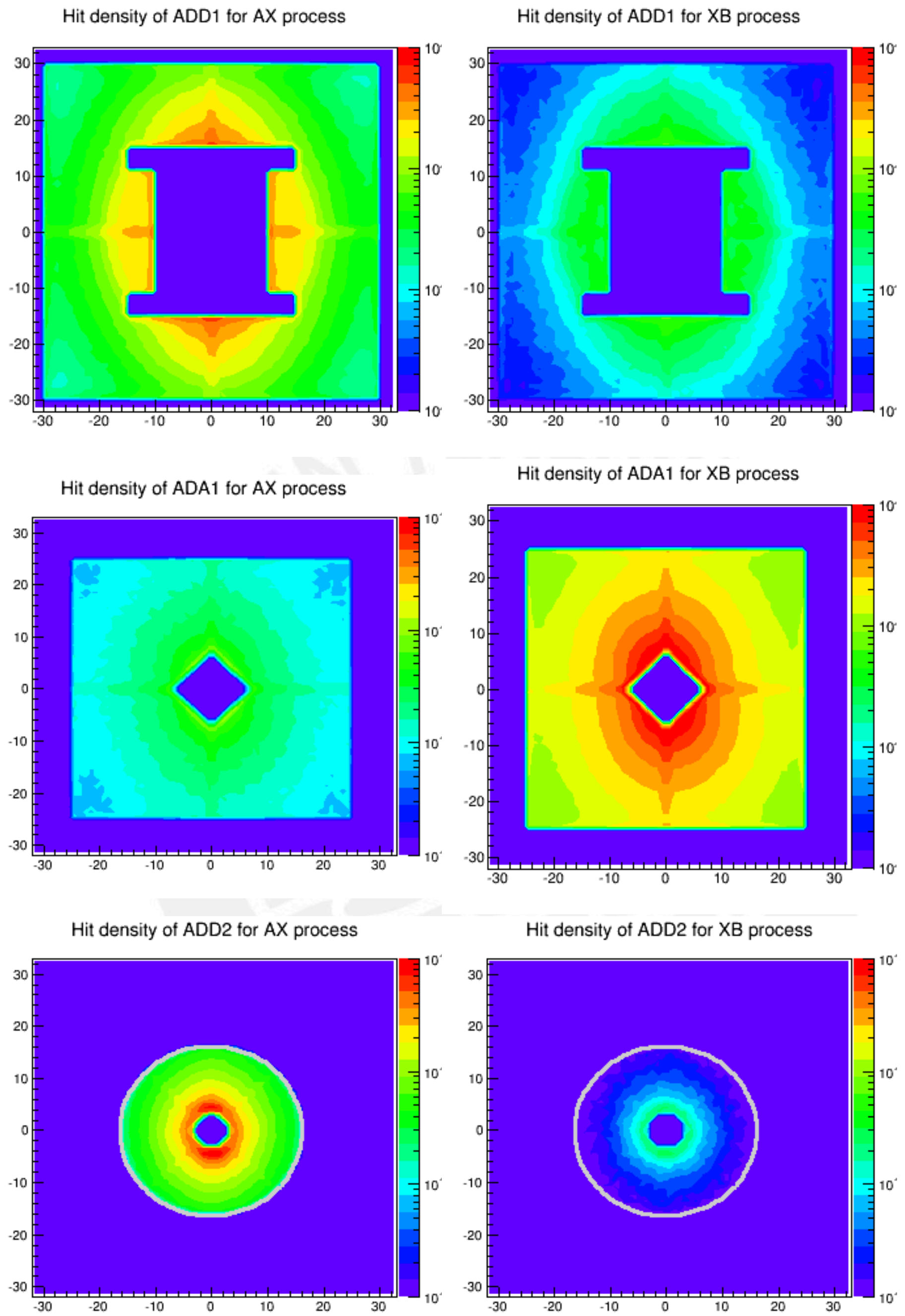

Figure 3.7: Average charged-hit density per event per squared centimeter on the first the AD stations at an energy of $\sqrt{s} = 7$ TeV. The top plots shows the ADC at $z = -1950$ cm for SD-L (top left) and SD-R (top right) diffractive events. The middle if for the ADA station (placed at $z = 1700$ cm) for SD-L (middle left) and SD-R (middle right). The bottom plot is for the ADC2 station (placed at $z = -2250$ cm) for SD-L (bottom left) and SD-R (bottom right)

Origin of Secondaries

The actual path of the particles from the interaction point to the detectors are not straight lines. Several elements determine the final trajectory of the particles. For example ALICE has a magnetic field of 0.5 Tesla in the direction parallel to the beam line which helps the central detectors of ALICE to determine the momentum of the particles. On the right (or A) side of ALICE there is a compensator magnet. The ADA station is located behind this magnet. Another source of intense magnetic field is located in the left (or C) side of ALICE where the muon spectrometer is located. This muon spectrometer (aka muon arm) has large amounts of absorber materials used to improve the quality of its measurements. The ADC station is located just 50 cm behind the last absorber material (a concrete block) of the muon arm.

This complicates the passage of primary particles while at the same time creates a lot of secondaries which helps to increase the efficiency of the detectors. The majority of the particles hitting the detectors are secondary particles originating from the decay of primary particles or from their interaction with the material elements inside the ALICE cavern. In fig. 3.8 we trace back the hits on the detectors due to secondary particles (i.e. those that were not physical primaries) drawing a pixel at the start of the parent track and iterate this procedure until we reach the mother primary track. As can be inferred from the figure, the secondary tracks came in all directions from the material objects surrounding the detectors.

In order to understand better the correlation between the rapidity of a primary particle coming from the collision and the secondary tracks that it generates, ultimately reaching the AD stations, we device the following procedure. For each secondary charged track hitting one AD station we compute the geometrical pseudorapidity of that track at the detector position by joining with a straight line the point of impact of the track on the detector to the collision vertex and then applying $\eta_{\mathrm{det}} = -\ln(\tan(\theta/2))$ to the angle formed by the beam axis and this line. Then, iterating over the stack of particles, we find the (physical) primary particle from which the secondary originated and calculate its rapidity using its momentum (η_{pri}) to finally plot the points (η_{det},η_{pri}) in fig. 3.9 for each AD station.

Due to the way in which it was defined, the geometrical pseudorapidity of the secondary tracks, in the x-axis of the plot, is constrained by the pseudorapidity coverage of the respective AD station. In an ideal case, with no magnetic fields and no material between the detectors and the interaction point we could expect that the $\eta_{\mathrm{det}} \simeq \eta_{\mathrm{pri}}$ (with some decays spoiling the equality) and therefore the points in the plot very close to the identity. But due to the action of the material and magnetic fields this is not what happens. Nevertheless in all cases we see hot spots near the identity line, meaning that even though the particles are smeared in their way to the AD stations, when a hit is received there is some high probability that the particles came from a primary particle with a pseudorapidity matching the rapidity coverage of the AD station.

The reason to calculate the geometrical pseudo-rapidity η_{det} for the secondary tracks in this way is in anticipation to the definition of pseudo-tracks for the analysis of single diffractive events in the next chapter.

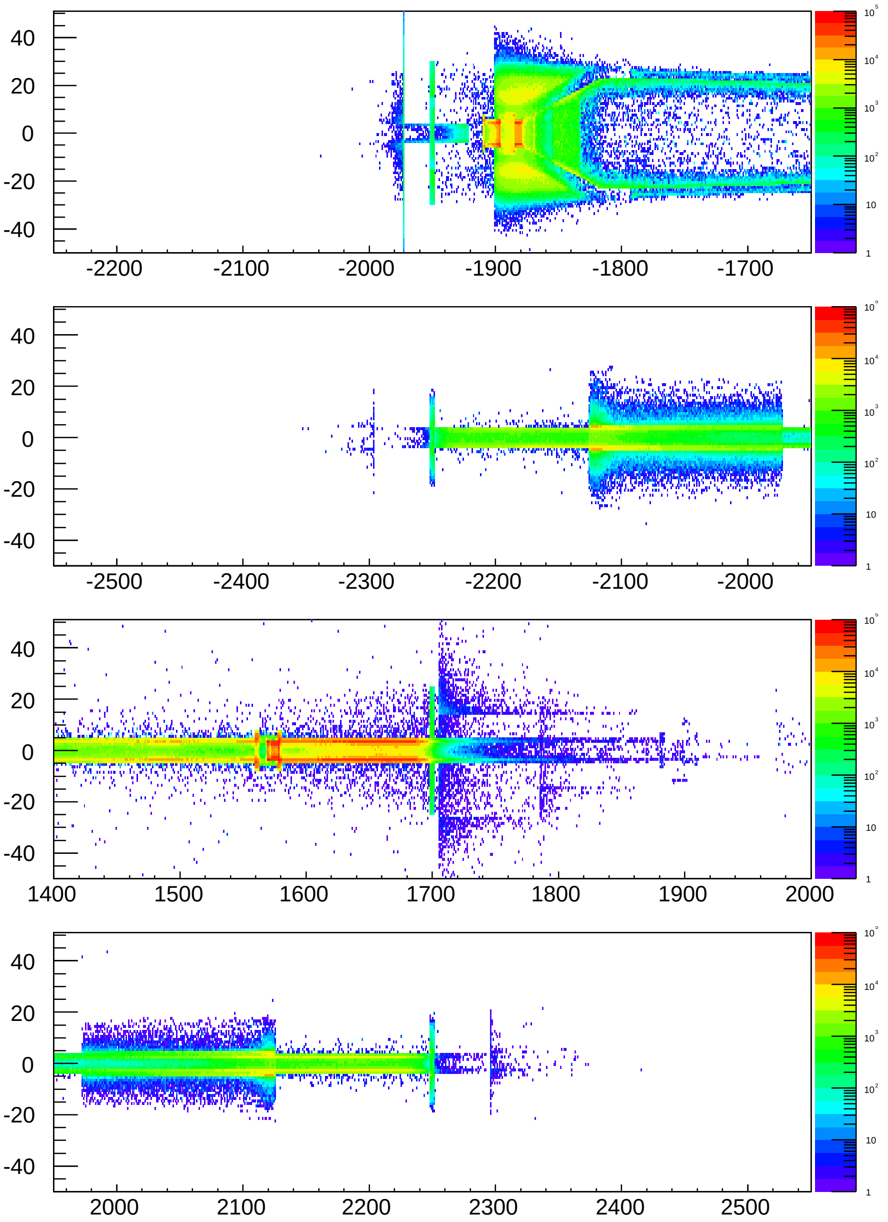

Figure 3.8: Projection on the Z-Y plane of the origin of secondary tracks hiting the AD stations ($\sqrt{s} = 7$ TeV). From top to bottom: ADC ($z = -1950$ cm), ADC2 ($z = -2250$ cm), ADA ($z = 1700$ cm), ADA2 ($z = -2250$ cm). All the axes units are in cm.

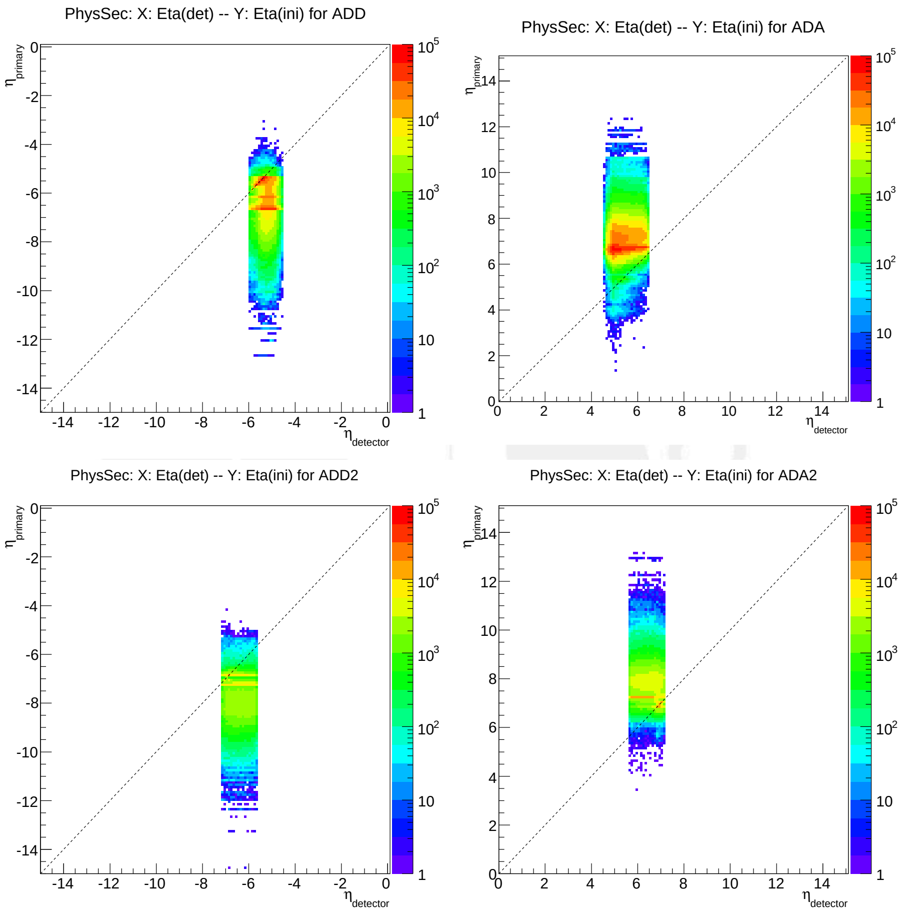

Figure 3.9: The points $(x, y) = (\eta_{\text{det}}, \eta_{\text{pri}})$ show the correlation between the pseudorapidity of the point of impact of a charged secondary track in the AD detector and the pseudorapidity of the primary track from which the secondary originates. Top left: ADC. Top right: ADA ($z = 17.0$ m). Bottom left: ADC2 ($z = 22.5$ m). Bottom right ADA2 ($z = -22.5$ m).

Stand-alone efficiency as function of diffracted mass

As seen in the previous chapter, there is a strong correlation between the mass of the excited system and the rapidity of the particles produced from it. At lower masses of this system, the particles are emitted more closely to the beam axis. It is natural to ask about the performance of the new AD detector for different values of the diffracted mass.

One way to evaluate this performance is to ask what fraction of the events will be seen by the detector. Since scintillators generate their signal by the light yield produced by traversing charged particles it is convenient to define the efficiency for the detector as:

$$\text{efficiency} = \frac{\#\text{ of events with at least a charged hit in the detector}}{\#\text{ of total events}} \tag{3.3.1}$$

Of the three configurations shown in table 3.1 the simulations show that the efficiency of the ADC2 and ADA2 stations at setup I ($z = \pm 55$ meters) was below 14% for diffracting processes sending particles in the direction of the detectors. This low efficiency can be explained by the big amount of material budget (several elements of the LHC such as magnets) the particles has to cross before reaching this stations. Furthermore these positions are outside the ALICE cavern and pertain to the LHC tunnel itself limiting the possibility of access to the detector.

In setup II we move the ADA2 and ADC2 stations to $z = \pm 22.5$ meters, where there is less material budged in the path of particles coming from interaction point, increasing their efficiency to about 70% (see table 3.2). This was accompanied by a change in the inner radius to tray to maintain the gain in rapidity coverage.

Finally in setup III of the simulation the ADA (initially at $z = 7.7$ m) was moved to $z = 17.0$ meters from the interaction point increasing the efficiency for the detector as well as the performance of the triggers in which it participates. In the following the results are centered in this last setup since it brings the major improvement.

In fig. 3.10 the efficiency of each AD station is plotted as a function of the diffracted mass for single diffractive events. Here the particles originated in the diffracted system are traveling towards the side where the detector is located.

In table 3.2 is displayed the total integrated efficiency of the AD stations to single diffractive events, at energies of 7 and 14 TeV, according to Pythia6 and Phojet, where the errors represent the statistical uncertainty computed by using four samples of 10^6 events. Over four independent samples are displayed. In addition the average of Pythia6 and Phojet is shown and systematic uncertainty estimated by the difference of this two values.

In figure 3.11 we display the total η coverage of the AD stations and other ALICE detectors, as determined in setup III.

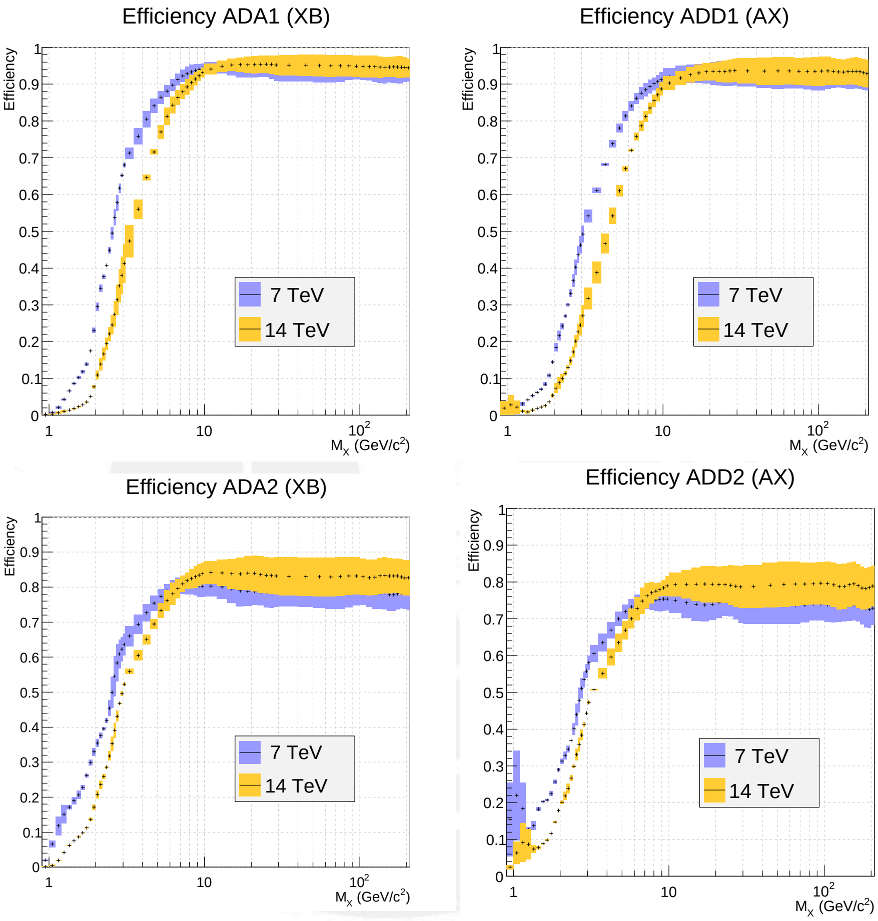

Figure 3.10: Comparison of efficiencies of AD stations for single diffractive processes of type SD-R (left) and SD-L (right) at $\sqrt{s} = 7$ (light blue) and $\sqrt{s} = 14$ TeV (pale yellow). Top left: ADA at $z = 17$ m, top right: ADC at $z = -19.5$ m, bottom left: ADA2 at $z = 22.5$ m, bottom left: ADC2 at $z = -22.5$ m.

Table 3.2: Efficiency of AD stations at $\sqrt{s}$ of 7 and 14 for single diffractive events where the diffracted mass is in the direction of the detector (SD-L for ADC and ADC2, SD-R for ADA and ADA2). For the rows labeled Pythia6 and Phojet we display the statistical error (σ_E). Then the average of these values is calculated and the statistical error estimated from the difference of Pythia6 and Phojet (the statistical error is ignored since it is negligible)

$\sqrt{s}$ (TeV)	generator	ADC (SD-L)	ADA (SD-R)	ADC2 (SD-L)	ADA2 (SD-L)
7.0	Pythia6	76.54 ± 0.11	80.32 ± 0.12	63.00 ± 0.09	67.81 ± 0.12
	Phojet	86.95 ± 0.05	88.97 ± 0.05	72.81 ± 0.05	77.00 ± 0.08
	Average	81.75 ± 5.21	84.65 ± 4.33	67.91 ± 4.91	72.41 ± 4.60
14.0	Pythia6	75.65 ± 0.06	79.32 ± 0.05	65.09 ± 0.16	69.15 ± 0.03
	Phojet	86.09 ± 0.11	87.85 ± 0.08	77.46 ± 0.04	80.32 ± 0.03
	Average	80.87 ± 5.22	83.59 ± 4.27	71.28 ± 6.19	74.74 ± 5.59

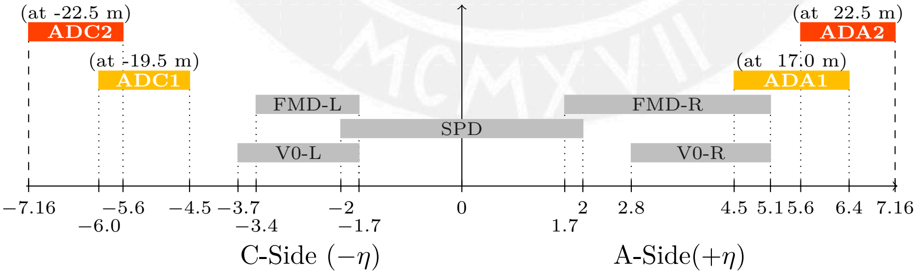

Figure 3.11: Pseudorapidity coverage of detectors used for diffractive triggers. In gray SPD, FMD and VZERO. In yellow proposed ADC ($z = -1950$ cm)and ADA ($z = 1700$ cm). In Orange proposed ADC2 ($z = -2500$ cm) and ADA2 ($z = +2500$ cm).

3.4 Effects of back scattering

The ADC station, situated at -19.5 meters from the interaction point, lays behind a concrete block that is part of the shielding of the muon triggers stations. The role of this shielding is to reduce the amount of back scattering on the muon trigger stations. It was suggested that removing of this block could be possible to improve the performance of the ADC station but studies should be needed to see the impact of this on the trigger stations. To this end, several simulations with the AliRoot framework and the full ALICE geometry were done for proton-proton minimum bias collisions using Pythia6 and Phojet generators and for several centrality lead-lead collisions using HIJING generator. Two set of simulation were done, the first with the standard materials for the concrete block and other with the medium of the concrete block replaced by air in the simulation.

The procedure for the analysis is as follows. First we define a forward particle as a particle hitting on any muon station and whose direction is away from the interaction point. We also define a backward particle as the one that hits muons station and whose directions is towards the interaction point.

Then, for each of the muon and trigger stations we compute the percent of back scattered particles for a certain material of the concrete block. This percent is simply the number of backward particles on a station over the total number of particles on the same station.

$$\%\mathrm{bk}^{\mathrm{station}}_{\mathrm{medium}} = \frac{\text{number of backward particles on station}}{\text{total number of particles on station}}$$

We do this for both cases, air and concrete, and then compare the percent of back scattering of each station in the case where the concrete block is removed (i.e. replaced by air) versus the case where this block is in place and with the standard materials.

Our results shows that the removal of the concrete block will increase significantly the backscattering on the first muon trigger station. The main source of backscattering is from pions, in lead-lead collisions.

Figure 3.12: Results Pb-Pb

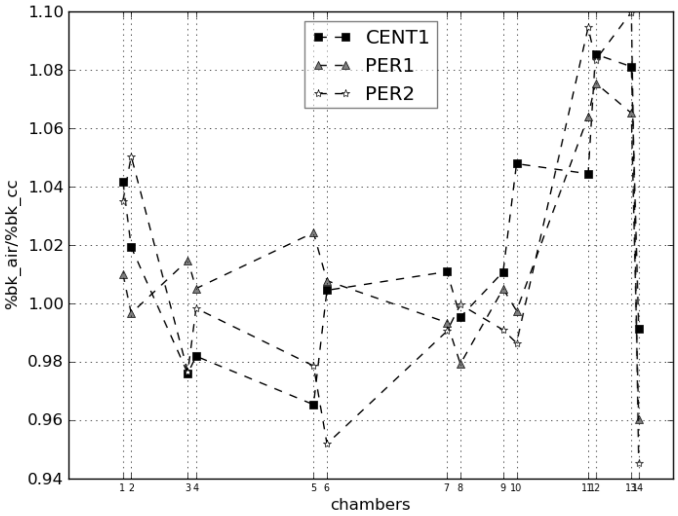

Chapter 4

Analysis and Results

4.1 Trigger Definitions

As mentioned in section 1.1.4, only events marked as “interesting” by the CTP are stored for further offline analysis. These decisions are made according to online trigger definitions. Here we define the relevant triggers for this diffractive physics.

4.1.1 Minimum Bias triggers

One of the main triggers of ALICE is the minimum bias trigger. Its mission is to select interaction events. It is defined requiring at least one hit in either **VZERO-A**, **VZERO-C** or **SPD**.

$$\text{MB-OR} \quad = \quad \text{V0A} \quad \vee \quad \text{SPD} \quad \vee \quad \text{V0C} \tag{4.1.1}$$

Here, the symbol $\vee$ stands for the logical OR. Another commonly used trigger is the MB-AND, requiring hits on both **VZERO-A** and **VZERO-C** arrays. This symmetrical condition on the VZERO detectors is used when we are interested in non single diffractive events (NSD).

After the events had been selected by a trigger, a further offline selection is usually done on the events. As we will see, offline triggers have been developed to select diffractive events with maximum efficiency with the available pseudorapidity coverage of the detectors. These offline triggers did a good job at high diffracted masses but failed at masses below 10 GeV/c^2. To overcome this issue, we evaluate new trigger definitions (*ad hoc* triggers) using the proposed AD detectors and also evaluate the performance of offline triggers used in a recent ALICE paper when the AD detectors are taken into account.

Using the standard ALICE MB-OR online trigger for data taking will cause the loss of events with tracks only at forward rapidities. In this scenario, a further offline analysis using AD signals will bring no enhancement since the events are lost to begin with.

It is important therefore to include the AD information in the data taking decision at the online level. This can be done by extending the MB_{OR} definition to use the AD stations or by defining *ad hoc* online triggers using logical combinations of activity in the AD stations and other standard detectors.

Following the first approach we defined the extended MB-OR online triggers as:

$$\begin{array}{lcrcccl} \text{MB-OR}_0 & = & \text{V0A} & \vee & \text{SPD} & \vee & \text{V0C} \\ \text{MB-OR}_1 & = & (\text{ADA} \vee \text{V0A}) & \vee & \text{SPD} & \vee & (\text{V0C} \vee \text{ADC}) \\ \text{MB-OR}_2 & = & (\text{ADA2} \vee \text{ADA} \vee \text{V0A}) & \vee & \text{SPD} & \vee & (\text{V0C} \vee \text{ADC} \vee \text{ADC2}) \end{array} \tag{4.1.2}$$

Below we defined triggers using the second approach.

4.1.2 ad hoc proposal for diffractive triggers

While extending the MB-OR will increase the selection of diffractive events it will also select a lot of non-diffractive events, therefore it would be convenient to have ad hoc triggers for this specific task. We define online triggers for single, double and central diffraction using activity on VZERO, SPD and the proposed AD stations.

We remind the reader about a few of the conventions introduced in section 3.1. We label as single diffractive event on the left side (SD-L) when the diffracted proton is going to the left side (C-side) of ALICE (i.e. negative pseudorapidity and z values). Similarly, we label events as single diffractive event on the right side (SD-R) when the diffracted proton is going to the right side (or A-side, positive pseudo-rapidities) of the experiment.

The naming convention for these triggers is to indicate by a subindex i the number of AD stations used (always according to setup III of table 3.1) in the following way: $i = 0$ means that **no AD stations** but only standard ALICE detectors. $i = 1$ means that in addition to the standard ALICE detectors, we are using the **two AD stations** closest to the interaction point (i.e. ADA and ADC); $i = 2$ means we are using all the **four AD stations** on top of the standard ones.

For diffraction on the left side we define:

$$\begin{array}{lcrcccl} \text{SD-L}_0 & = & \sim \text{V0A} & \wedge & \sim \text{SPD} & \wedge & \text{V0C} \\ \text{SD-L}_1 & = & \sim (\text{ADA} \vee \text{V0A}) & \wedge & \sim \text{SPD} & \wedge & (\text{V0C} \vee \text{ADC}) \\ \text{SD-L}_2 & = & \sim (\text{ADA2} \vee \text{ADA} \vee \text{V0A}) & \wedge & \sim \text{SPD} & \wedge & (\text{V0C} \vee \text{ADC} \vee \text{ADC2}) \end{array} \tag{4.1.3}$$

Where $\sim$ is the logical NOT (no hit on detector), $\vee$ is logical OR and $\wedge$ is logical AND. In the case of the diffracted proton is going to the right side of the detector (i.e. positive pseudorapidity and z values, A-side) we define the following ad hoc triggers:

$$\begin{array}{lcrcccl} \text{SD-R}_0 & = & \text{V0A} & \wedge & \sim \text{SPD} & \wedge & \sim \text{V0C} \\ \text{SD-R}_1 & = & (\text{ADA} \vee \text{V0A}) & \wedge & \sim \text{SPD} & \wedge & \sim (\text{V0C} \vee \text{ADC}) \\ \text{SD-R}_2 & = & (\text{ADA2} \vee \text{ADA} \vee \text{V0A}) & \wedge & \sim \text{SPD} & \wedge & \sim (\text{V0C} \vee \text{ADC} \vee \text{ADC2}) \end{array} \tag{4.1.4}$$

Then the condition for single diffractions can be expressed as

$$\begin{array}{lclcl} \text{SD}_0 & = & \text{SD-L}_0 & \| & \text{SD-R}_0 \\ \text{SD}_1 & = & \text{SD-L}_1 & \| & \text{SD-R}_1 \\ \text{SD}_2 & = & \text{SD-L}_2 & \| & \text{SD-R}_2 \end{array} \tag{4.1.5}$$

The triggers for double diffraction (DD_i) are:

$$\begin{array}{lcrcccl}
\mathrm{DD}_0 & = & \mathrm{V0A} & \wedge & \sim \mathrm{SPD} & \wedge & \mathrm{V0C} \\
\mathrm{DD}_1 & = & (\mathrm{ADA} \vee \mathrm{V0A}) & \wedge & \sim \mathrm{SPD} & \wedge & (\mathrm{V0C} \vee \mathrm{ADC}) \\
\mathrm{DD}_2 & = & (\mathrm{ADA2} \vee \mathrm{ADA} \vee \mathrm{V0A}) & \wedge & \sim \mathrm{SPD} & \wedge & (\mathrm{V0C} \vee \mathrm{ADC} \vee \mathrm{ADC2})
\end{array} \tag{4.1.6}$$

and for central diffraction (CD).

$$\begin{array}{lcrccl}
\mathrm{CD}_0 & = & \sim \mathrm{V0A} & \wedge \mathrm{SPD} & \wedge & \sim \mathrm{V0C} \\
\mathrm{CD}_1 & = & \sim (\mathrm{ADA} \vee \mathrm{V0A}) & \wedge \mathrm{SPD} & \wedge & \sim (\mathrm{V0C} \vee \mathrm{ADC}) \\
\mathrm{CD}_2 & = & \sim (\mathrm{ADA2} \vee \mathrm{ADA} \vee \mathrm{V0A}) & \wedge \mathrm{SPD} & \wedge & \sim (\mathrm{V0C} \vee \mathrm{ADC} \vee \mathrm{ADC2})
\end{array} \tag{4.1.7}$$

4.1.3 1-arm-L(R)/2-arm triggers

The ALICE collaboration reports in a recent paper [23] the measurement of single-, double- and inelastic cross section using special offline trigger definitions, 1-arm-L, 1-arm-R and 2-arm. These triggers or selections analyze the gap topology using hits from SPD, VZERO and FMD in such a way that the 1-arm-L trigger has a preference for single diffracted events of type SD-L, 1-arm-R has a preference for single diffraction SD-R, and the 2-arm category picks up non diffractive and double diffractive events. Nevertheless the efficiency of the 1-arm-L (1-arm-R) selections fall quickly for low diffracted mass where according to several models, the majority of the production occurs.

Below we show the definition of the triggers and later we study how adding the AD stations improves their efficiency at low diffracted masses. When presenting results comparing the performance of this triggers we will continue to use the convention for *ad hoc* triggers defined in section section 4.1.2

Pseudo-tracks

For this offline trigger selection the base elements are the so called *pseudo-tracks*, which are straight virtual segments constructed by joining the hits or points of impact of the charged particles on the detectors and the interaction vertex of the collision as estimated by the SPD.

In case the detector can't tell the point of impact (as is the case for scintillators like VZERO and the AD's) the pseudo-track is generated by choosing a random point in the fired element of the detector and joining that point to the vertex. In the analysis of real events it may happen that there is no reconstructed vertex, in this case a random vertex is used from the vertex distribution of the run being analyzed. In the analysis of simulated transported data we always have the information of the vertex from the Monte Carlo.

Then, using these pseudo-tracks, we first classify the events as single-track and multi-track. For this, let η_R be the pseudorapidity of the particle with the highest (rightmost) pseudorapidity in the event, and η_L that of the particle with the lowest (leftmost) pseudorapidity.

Single-track events

An event is single-track if and only if all the pseudo-tracks are in the pseudorapidity range $\eta_R - \eta_L < 0.5$ and the azimuthal angle ϕ of all of them is within 45 degrees. If this condition is not fulfilled the event is said to be multi-track. This of course means that any event having only one pseudo-track is also single-track. Then for single-track events we define the center of pseudorapidity distribution (η_C) as:

$$\eta_C = \frac{1}{2}(\eta_R + \eta_L)$$

Then with this information we classify the events as:

- 1-arm-L, if $\eta_C < 0$
- 1-arm-R, if $\eta_C > 0$

Multi-track events

As mentioned above, multi-track events are those that were not classified as single-track events. For the gap analysis of multi-track events we define (see fig. 4.1) d_L as the distance (in pseudorapidity) from the lower end of the pseudorapidity coverage of the detectors to the particle with the lowest pseudorapidity in the event η_L. In a similar way lets define d_R as the pseudorapidity interval from the particle with the highest pseudorapidity (η_R) to the upper end of the pseudorapidity acceptance of the detectors used in the analysis. It is worth noting at this point that the edges of the pseudorapidity coverage of the detectors will change as we add the AD stations to the analysis. Lets also define $\Delta\eta$ as the largest pseudorapidity gap between two adjacent tracks in the event.

With this information we classify the multi-track events in the following way:

- If the largest gap $\Delta\eta$ is larger than both d_L and d_R, the event is termed **2-arm**. This way we pick up events with a central gap.
- if both η_L and η_R are in the interval $-1 \leq \eta \leq 1$ the event is **2-arm**, otherwise, if $\eta_R < 1$ the event is **1-arm-L**, else if $\eta_L > -1$ the event is

Figure 4.1: Definition of 1-arm-L(R)/2-arm triggers for multi-track events. The pseudorapidity coverage of relevant detectors is shown in color boxes. For the AD stations their z position is also shown.

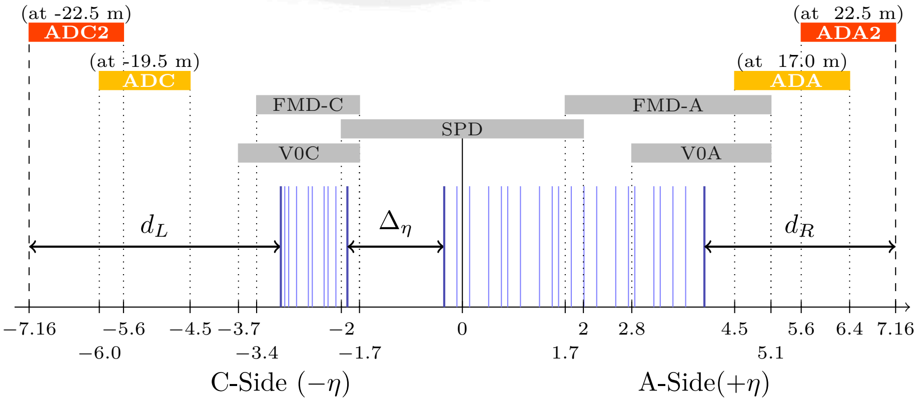

1-arm-R. Here the first condition tell us to identify as 2-arm any event where there is no a preference of the particles to populate one side of the coverage of the detectors. After the first condition, the second one tags as 1-arm-L the events where the distribution of particles have their leftmost edge to the left of $\eta = -1$ and the rightmost edge to the left of $\eta = 1$, i.e. spread to the left of $\eta = 1$ or equivalently with a gap on the right of $\eta = 1$. Analogously the third condition tag as 1-arm-R events where both edges of the particle distribution are to the right of $\eta = -1$, i.e. a gap to the left of $\eta = -1$.

- any other event is classified as **2-arm**.

In this way this classification makes the 1-arm-L and 1-arm-R to have an enriched component of single diffractive events, while the 2-arm picks up double-diffractive and non-diffractive events. To select double diffractive events it is required that the event is tagged as a 2-arm event and that the size of the largest gap in this event to be greater than three units of pseudorapidity ($\Delta\eta > 3$).

4.1.4 Using the AD stations with 1-arm-L(R)/2-arm selections

The standard definition of the just reviewed selections uses pseudo-tracks from VZERO, SPD and FMD detectors providing a pseudorapidity coverage of $-3.7 < \eta < 5.1$. The idea on how to improve this analysis is to include the pseudo-tracks from two (ADC and ADA) and four AD stations extending the pseudo-rapidity range covered by the selection to $-6.0 < \eta < 6.4$ and $-7.16 < \eta < 7.16$ respectively.

4.1.5 Online versus Offline selection

The 1-arm-L(R)/2-arm event categories we have just defined are offline triggers. This means they are not used at the online level where the decision on what events are recorded is made. Rather the events are first recorded by some of the online triggers (e.g. the minimum bias triggers MB-OR) and then the analysis with the 1-arm-L(R)/2-arm triggers is done over these events.

In this case the trigger of choice is the standard minimum bias. Nevertheless, it can be anticipated that using the enhanced 1-arm-L(R)/2-arm selections on data taken by the standard minimum bias (defined using only SPD and VZERO) will produce no improvement. This is confirmed by analysis of our simulations, preselecting the events with standard $\mathrm{MB_{OR}}$ and then applying the 1-arm-L(R)/2-arm selections. In fact, there is a small deterioration of the efficiency.

To overcome this issue and to present a more realistic analysis case, in the following, whenever we mention the 1-arm-L(R)/2-arm triggers we really meant the coupling of the extended minimum bias $\mathrm{MB}^{\mathrm{OR}}_{(i)}$ online trigger together with the respective 1-arm-L(R) $_{(i)}$ or 2-arm $_{(i)}$ offline selection. As mention before, the sub-indexes indicates if we are using only standard ALICE detectors ($i = 0$), or if in addition we use two($i = 1$) or four ($i = 2$) AD stations.

4.2 Efficiency of triggers as function of diffracted masses

Here efficiency is the fraction of events selected by the trigger when exposed to a pure sample of diffractive events of the exact type it is supposed to select.

$$\mathrm{Eff}_{\mathrm{trigger\ X}} = \frac{\#\ \text{selected events}}{\#\ \text{total events in pure sample of type X}} \tag{4.2.1}$$

In fig. 4.2 the efficiency of the 1-arm-L(R) triggers (defined in section 4.1.3) is plotted as a function of the mass of the diffracted system. The top and bottom plots corresponds to an energy collision of $\sqrt{s} = 7$ and $\sqrt{s} = 14$ TeV respectively. The left and right half of the figures show the efficiency of the 1-arm-L (left) 1-arm-R (right) in selecting SD-L and SD-R events respectively. The red boxes show this efficiency when using only SPD, VZERO and FMD having a joint rapidity coverage of $-3.7 < \eta < 5.1$.

As seen in section 2.4.1, in single diffracted events, the lowest rapidity (in absolute value) of a particle originating from the diffracted proton is roughly $|y| \simeq |\eta| \simeq \ln(m\sqrt{s}/M^2)$, this means that the lower the mass of diffracted system, the higher (in absolute value) its rapidity. In consequence the particles are emitted closer to the beam pipe. This can also be seen in fig. 4.3 where we plot the pseudo-rapidity of particles and the mass of the diffracted system for a sample of pure SD-L and SD-R events.

Therefore, we expect to lose events at diffracted masses below 10 GeV/c^2. This is actually the case as can be seen in the plots. Note in particular that at $\sqrt{s} = 7$ TeV (fig. 4.2, top plots, red boxes) the efficiency in selecting diffractive events falls below 50% at masses $M_X < 14$ (8) GeV/c^2 for SD-L (SD-R) and below 20% when $M_X < 5.5$ (10) GeV/c^2 for SD-L (SD-R).

On the other side of the mass spectrum, the efficiency is below 50% when $M_X > 170$ GeV/c^2 for both SD-R and SD-L events. This can be explained considering fig. 4.3. We see that at higher diffracted mass the pseudo rapidity of the particles reach $\eta = 0$ and can even cover completely the pseudo-rapidity coverage of the detectors used in the analysis ($-3.7 < \eta < 5.1$). So, even though there is a gap between the particles and the surviving proton, it lies outside the coverage of the detectors and therefore can not be detected. Note also that in this region, the curves for the cases $i = 0, 1, 2$ coincide almost perfectly, even though for each curve we have different pseudorapidity coverage (due to the addition of AD stations). What is more, this part of the curve is very similar for SD-L and SD-R processes. This can be understood by remembering the definition of 1-arm-L and 1-arm-R events for multi-track events section 4.1.3. Here 1-arm-L events are those multi-track events whose rightmost edge is to the left of $\eta = 1$. This condition does not change with the addition of AD stations. Similarly for 1-arm-R events the condition is that the left edge of the distribution is to the right of $\eta = -1$. As can be seen in fig. 4.3 events having a diffracted mass of 100 GeV/c^2 start to fail this condition for both cases.

There is a noticeable asymmetry (using current ALICE detectors) at low diffracted masses in the efficiency curve for SD-L and SD-R. This is due to the asymmetry in the edges of the rapidity coverage and can be understood considering again fig. 4.3: For SD-R events, the right (or upper) edge of the coverage

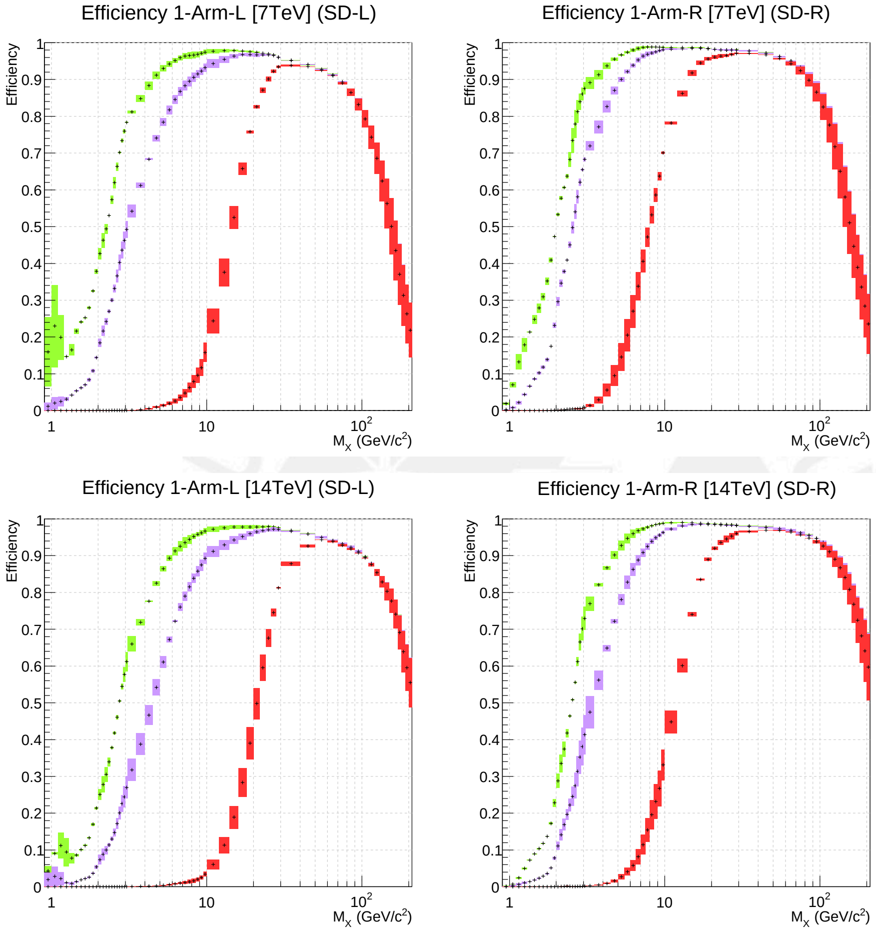

Figure 4.2: Comparison of the selection efficiency as function of diffracted mass for single diffractive events at $\sqrt{s} = 7$ TeV (top) and $\sqrt{s} = 14$ TeV (bottom). Left: efficiency of 1-arm-L in selecting SD-L events. Right: efficiency of 1-arm-R in selecting SD-R events. Red boxes shows the current situation using only standard ALICE detectors (VZERO, SPD, FMD). Violet boxes uses in addition two AD counter stations (ADA and ADC). The green curve is using standard ALICE and all the four AD counter stations (ADA, ADC, ADA2, ADC2). The boxes show the systematic uncertainties estimated from the differences between Pythia6 and Phojet.

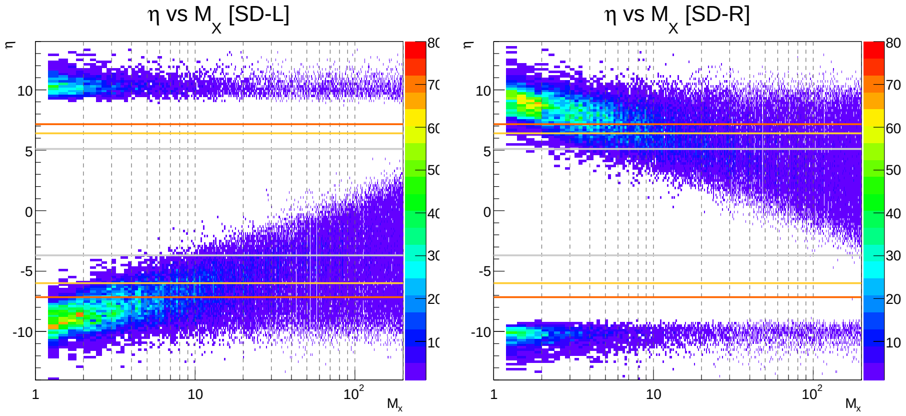

Figure 4.3: Pseudorapidity of particles versus diffracted mass of the parent system for single diffractive events of type SD-L (left) and SD-R (right) according to Pythia6 for an energy of 7.0 TeV. The horizontal lines show the η coverage for: SPD+VZERO+FMD (grey), plus two (yellow) and four (orange) AD stations. For SD-L (SD-R) the patch at $\eta \sim 10$ ($\eta \sim -10$) is due to the non-diffracted proton.

($\eta = 5.1$) is closest to the rapidity span of the diffracted system compared to the distance between the left (or lower) edge of coverage of detectors ($\eta = -3.7$) and the right edge of the diffracted system in SD-L events.

The efficiency improves dramatically by adding two AD stations to the previous set up (violet boxes in fig. 4.2). The rapidity coverage is extended to $-6.0 < \eta < 6.4$ which results in a increase in the sensitivity to low mass diffracted events. In particular note that at 7 TeV the efficiency falls below 50% at masses $M_X < 3.0$ (2.5) GeV$/c^2$ for SD-L (SD-R) and below 20% when $M_X < 2.1$ (1.9) GeV$/c^2$ for SD-L (SD-R).

When the four AD stations are incorporated (green boxes) to the analysis a modest improvement is observed with respect to the two station case. Here the pseudo-rapidity coverage is extended to $-7.16 < \eta < 7.16$ and can be observed that (at 7 TeV) the efficiency falls below 50% for masses $M_X < 2.2(2.0)$ GeV$/c^2$ for SD-L (SD-R) and below 20% whenever $M_X < 1.4(1.3)$ GeV$/c^2$ for SD-L (SD-R).

A similar situation occurs at $\sqrt{s} = 14$ TeV. From eq. (2.4.21) we can see that at higher energies the products of the break-up of the diffractive system are emitted with higher (in absolute value) rapidities (i.e. closer to the beam pipe). This has the effect of displacing the efficiency curves to the right (fig. 4.2, bottom) where the efficiency fall below 50% for $M_X < 20$ (12) GeV$/c^2$ for SD-L (SD-R). Adding two (violet boxes) and four (green boxes) AD stations improves the efficiency of the 1-arm-L(R)/2-arm selections as in the case before.

For the ad hoc triggers (see fig. 4.4) the form of the cutoff at high masses is dominated by the condition of no hits on SPD. For SD-L (SD-R) this causes events with tracks at $\eta > -2$ ($\eta < 2$) to be rejected. Hence the efficiency begins to drop for values higher than $M_X \approx 30$ GeV$/c^2$.

Remarkably, the shape of the curves below $M_X \approx 20$ GeV$/c^2$ are identical

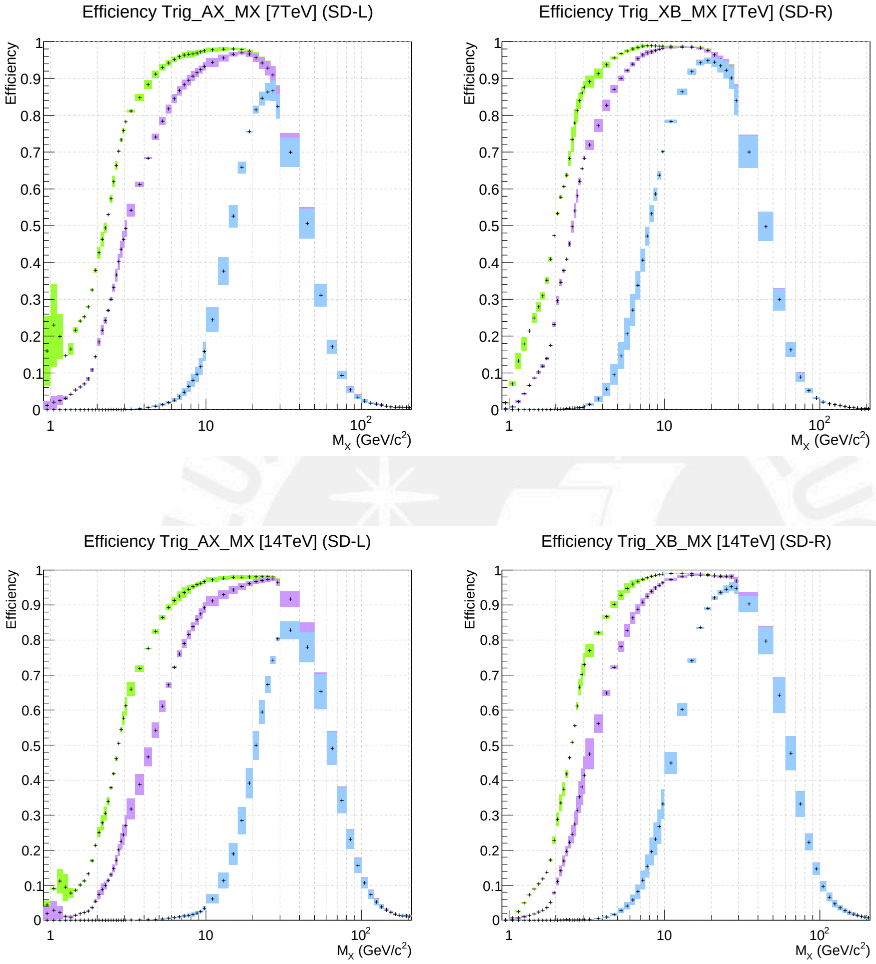

Figure 4.4: Comparison of the selection efficiency of *ad hoc* triggers as function of diffracted mass for single diffractive events at $\sqrt{s} = 7$ TeV (top) and $\sqrt{s} = 14$ TeV (bottom). Left: efficiency of SD-L trigger in selecting SD-L events. Right: efficiency of SD-R trigger in selecting SD-R events. light blue boxes shows the current situation using only standard ALICE detectors (VZERO, SPD, FMD). Violet boxes uses in addition two AD counter stations (ADA and ADC). The green curve is using standard ALICE and all the four AD counter stations (ADA, ADC, ADA2, ADC2). The boxes show the systematic uncertainties estimated from the differences between Pythia6 and Phojet.

to the efficiency curves for 1-arm-L(R)/2-arm triggers. For the SD-L case, this can be understood by remembering that the definition of multi-track events tags as 1-arm-L those events having all its tracks to the left of $\eta = 1$. The ad hoc trigger use instead the condition of having only hits in any of V0C, ADC or ADC2 and none in SPD, ADA nor ADA2. This is equivalent to require to have all the track to the left of $\eta = -2$ (left edge of SPD pseudorapidity coverage). For events where all the tracks have $\eta < -2$ (and in consequence low diffracted mass) the two definitions are equivalent. A similar argument applies to SD-R events.

4.3 Efficiency of Minimum bias triggers as function of event multiplicity

In eq. (4.1.1) we defined the minimum bias trigger, and in eq. (4.1.2) we extend the MB-OR definition to increase its pseudorapidity coverage using the AD stations. Now in this section we analyze the efficiency of these trigger definitions. In table 4.1 we show the efficiency of these extended MB-OR triggers at $\sqrt{s} = 14$ TeV in selecting different event types (diffractive and non diffractive). The efficiency is defined as before (the fraction of selected events from a pure sample) and is computed at the hit level taking into account the full ALICE geometry as described by the AliRoot framework. In table 4.2 we show the results for MB-OR trigger at $\sqrt{s} = 14$ TeV. There is an almost unnoticeable decrease in the efficiency for diffractive processes in comparison to $\sqrt{s} = 7$ TeV while there is no variation for non diffractive processes. Then, in table 4.3, we show the total fraction of events selected by these triggers when confronted to a minimum bias sample.

We can see that the standard MB-OR trigger of ALICE already selects 94% of the total of events in a minimum bias sample, and it is highly efficient in selecting non diffractive events (which constitute the largest fraction in a minimum bias sample). Nevertheless it only selects about 70 percent of SD-L and SD-R diffractive events whose tracks happen to fall in the rapidity coverage of SPD and VZERO. A moderate improvement is achieved in the collection of single and double diffractive events by using two stations (ADC and ADA) and four (ADC, ADA, ADC2, ADA2) stations while maintaining the efficiency for non diffractive events. Since the standard MB-OR trigger already selects 94% of all events, extending its definition will not suppose an excessive increase in the trigger rate nor will result in an overload to the CTP.

In fig. 4.5 we show, for different process types, how the efficiency of the standard and extended MB-OR triggers behave as a function of the total multiplicity of the event (the total number of primary tracks extracted from `AliStack`). We observe that for standard MB-OR, the saturation is reached for multiplicities of about 40 tracks for SD-L and DD, 30 for SD-R, and 25 for CD. The difference between SD-L and SD-R is explained by the asymmetry of the pseudorapidity coverage of the V0A and V0C detectors. Using ADA and ADC brings a noticeable increase on the efficiency of MB-OR, which now reach the saturation point at lower multiplicities. Finally the addition of ADA2 and ADC2 brings an additional but marginal increase in performance. For single-diffractive events, the lower the value of the diffracted mass (M_X) the more close to the beam

Table 4.1: Efficiency of *minimum bias* trigger in selecting different types of pure events using Pythia6 and Phojet at $\sqrt{s} = 7$. Note that Pythia6 does not implement central diffraction (CD).

trigger	Generator	SD-L	SD-R	DD	CD	ND
		Efficiency(%) $\sqrt{s} = 7$ TeV				
MB-OR$_0$	Pythia6	69.60	75.19	87.30	–	99.96
MB-OR$_1$		84.65	87.48	96.96	–	100.00
MB-OR$_2$		89.80	91.35	98.67	–	100.00
MB-OR$_0$	Phojet	76.26	81.32	94.31	96.18	99.98
MB-OR$_1$		90.77	92.55	99.28	99.10	100.00
MB-OR$_2$		94.27	95.10	99.73	99.31	100.00

Table 4.2: Efficiency of *minimum bias* trigger in selecting different types of pure events using Pythia6 and Phojet at $\sqrt{s} = 14$ TeV. Note that Pythia6 does not implement central diffraction (CD).

trigger	Generator	SD-L	SD-R	DD	CD	ND
		Efficiency(%) $\sqrt{s} = 14$ TeV				
MB-OR$_0$	Pythia6	69.29	74.32	86.45	–	99.96
MB-OR$_1$		82.94	85.61	95.95	–	100.00
MB-OR$_2$		87.89	89.33	97.84	–	100.00
MB-OR$_0$	Phojet	74.76	79.22	93.02	94.53	99.99
MB-OR$_1$		88.99	90.41	98.75	98.95	100.00
MB-OR$_2$		92.89	93.32	99.46	99.32	100.00

Table 4.3: Total Efficiency of MB-OR$_i$ triggers in selecting minimum bias events at $\sqrt{s} = 7$ TeV and $\sqrt{s} = 14$ TeV. The error displayed show the systematic uncertainty estimated using Pythia6 and Phojet.

	Total Efficiency(%)	
trigger	$\sqrt{s} = 7$ TeV	$\sqrt{s} = 14$ TeV
MB-OR$_0$	94.93 ± 1.80	94.89 ± 1.68
MB-OR$_1$	97.89 ± 0.93	97.62 ± 0.97
MB-OR$_2$	98.64 ± 0.61	98.37 ± 0.70

are emitted the products of the diffracted proton. This implies lower efficiency of the MB-OR trigger due to pseudorapidity coverage. Also, a low diffracted mass is correlated with low number of tracks from the diffracted proton. It is consistent then, to have less efficiency for SD-L and SD-R at low multiplicities. In fig. 4.6 we show the corresponding plots for $\sqrt{s} = 14$ TeV. We can see that with high energies, the efficiency of the MB-OR triggers is reduced. The reason for this is that at higher energies the tracks from the diffracted system are boosted at more forward pseudorapidities. However, adding the AD stations to the trigger definitions, compensates for this effect, making the differences between $\sqrt{s} = 7$ and $\sqrt{s} = 14$ TeV almost marginal.

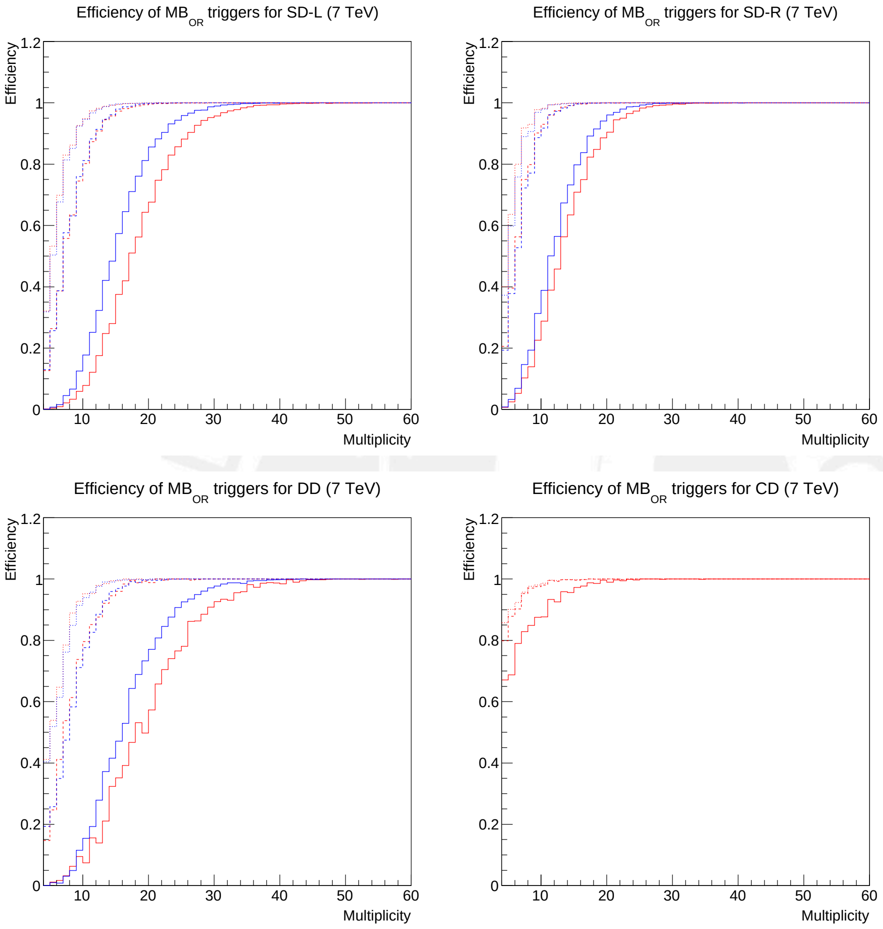

Figure 4.5: Efficiency in selecting diffractive events as function of multiplicity for MB-OR$_{(0,1,2)}$ triggers at $\sqrt{s} = 7$ TeV according to Pythia6 (blue) and Phojet (Red). Top left: SD-L. Top right: SD-R. Bottom left: double-diffraction. Bottom right: central diffraction. The solid lines depict the current situation (MB-OR$_0$). The dashed and dotted lines shows the situation when we add two (MB-OR$_1$) and four (MB-OR$_2$) AD stations to the definition of MB-OR.

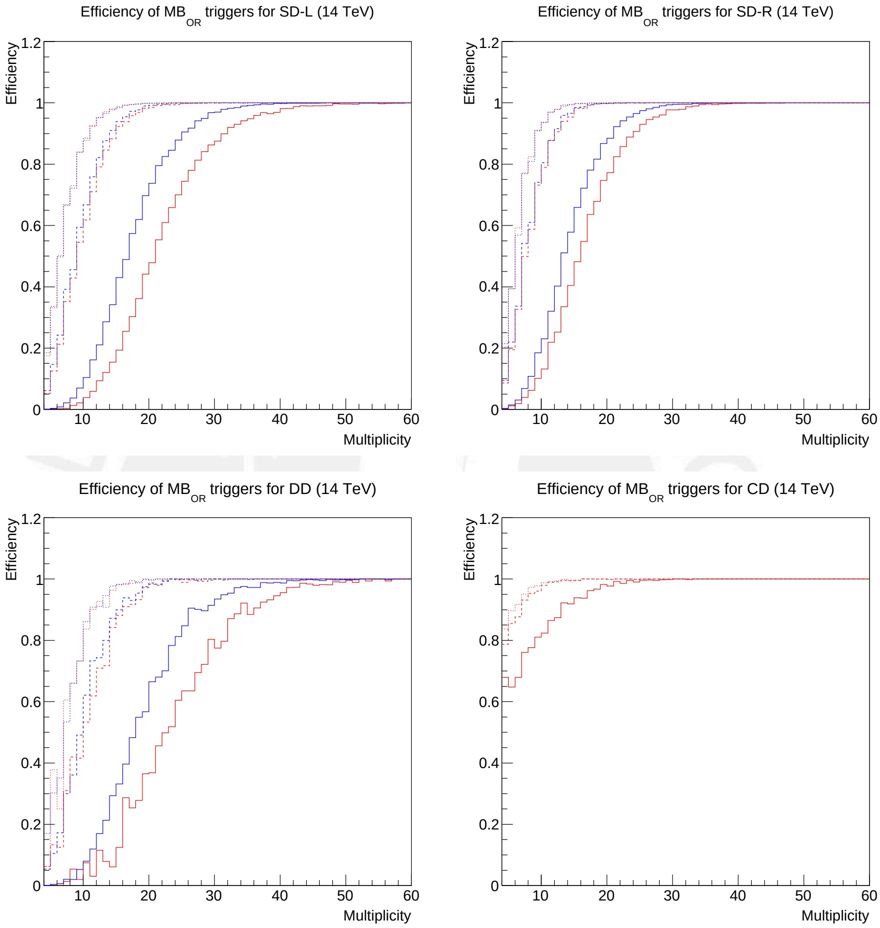

Figure 4.6: Efficiency in selecting diffractive events as function of multiplicity for MB-OR$_{(0,1,2)}$ triggers at $\sqrt{s} = 14$ TeV according to Pythia6 (blue) and Phojet (Red). Top left: SD-L. Top right: SD-R. Bottom left: double-diffraction. Bottom right: central diffraction. The solid lines depict the current situation (MB-OR$_0$). The dashed and dotted lines shows the situation when we add two (MB-OR$_1$) and four (MB-OR$_2$) AD stations to the definition of MB-OR.

4.4 Total efficiency and purity of diffractive triggers

Until now we have tested the triggers defined in section 4.2 only against pure events of the type they are designed to select. Nevertheless, in a real data taking scenario (whether they are used online or offline) the triggers will be confronted with events of all classes and they will have to accept with maximum efficiency the events they are designed to chase, while rejecting all other events. In this way, a selection of events with minimum contamination (event of type Y misidentified as X) and the highest purity possible, is created.

In order to quantify this, lets define the purity of a sample selected by a trigger as the ratio:

$$\text{Purity}_{(\text{trigg X})} = \frac{\#\text{ true events X in selected sample}}{\#\text{ total events selected by trigger}} \tag{4.4.1}$$

Monte Carlo generators try to reproduce the diversity of real events samples by generating mixtures of different event classes (SD-L, SD-R, DD, ND) in a definite proportion (the proportions or fractions vary with energy and correspond to the cross section for the production of events of each class). These mixtures are called minimum bias samples. The total number of events in a minimum bias sample (N_{MB}) is the sum of events of each class in the sample.

$$N_{\text{MB}} = N_{\text{diffractive}} + N_{\text{non-diffractive}} \tag{4.4.2}$$

$$N_{\text{MB}} = N_{\text{SD-L}} + N_{\text{SD-R}} + N_{\text{CD}} + N_{\text{DD}} + N_{\text{ND}} \tag{4.4.3}$$

Now, the number of events selected from a minimum bias sample by a trigger is:

$$\begin{pmatrix} \#\text{ total events} \\ \text{selected by} \\ \text{trigger X} \end{pmatrix} = P^X_{\text{SD-L}} N_{\text{SD-L}} + P^X_{\text{SD-R}} N_{\text{SD-R}} + P^X_{\text{CD}} N_{\text{CD}} + P^X_{\text{DD}} N_{\text{DD}} + P^X_{\text{ND}} N_{\text{ND}} \tag{4.4.4}$$

Where $P^X_{\text{SD-L}}$, $P^X_{\text{SD-R}}$, P^X_{DD}, P^X_{CD} and P^X_{ND} are the probability for the trigger X in selecting events of type SD-L, SD-R, DD, CD, ND respectively. This probabilities P^X_Y can be obtained by analyzing what fraction of events are selected by the trigger X when confronted with a pure sample of events of type Y. Using eqs. (4.4.1) and (4.4.4) we can calculate the purity of the trigger selection from a minimum bias sample knowing the probabilities P^X_Y. For example, the purity of the selection of SD-L from a minimum bias sample is:

$$\text{Purity}_{(\text{SD-L})} = \frac{P^X_{\text{SD-L}} N_{\text{SD-L}}}{P^X_{\text{SD-L}} N_{\text{SD-L}} + P^X_{\text{SD-R}} N_{\text{SD-R}} + P^X_{\text{DD}} N_{\text{DD}} + P^X_{\text{CD}} N_{\text{CD}} + P^X_{\text{ND}} N_{\text{ND}}} \tag{4.4.5}$$

In the particular case when $X = Y$ we call the probability P^X_Y as efficiency (eff_X) of the trigger. Dividing the numerator and denominator of eq. (4.4.5) by the number of minimum bias events in the input sample N_{MB} we have:

$$\text{Purity}_{(\text{SD-L})} = \frac{eff_{\text{SD-L}} f_{\text{SD-L}}}{P^X_{\text{SD-L}} f_{\text{SD-L}} + P^X_{\text{SD-R}} f_{\text{SD-R}} + P^X_{\text{DD}} f_{\text{DD}} + P^X_{\text{CD}} f_{\text{CD}} + P^X_{\text{ND}} f_{\text{ND}}} \tag{4.4.6}$$

where $f_{\text{SD-L}}$, $f_{\text{SD-R}}$, f_{DD}, f_{CD} and f_{ND} represent the fraction of events of each type in the minimum bias sample. The values of this fractions are displayed in table 4.4. Note that there is no central diffraction in Pythia6.

Table 4.4: Composition of a sample of *minimum bias* events according to Pythia6 and Phojet. Note that Pythia6 does not implement central diffraction (CD).

$\sqrt{s}$ (TeV)	generator	SD-L(%)	SD-R(%)	DD(%)	CD(%)	ND(%)
7	Pythia6	9.57	9.57	12.28	–	68.58
14	Pythia6	9.03	9.03	12.28	–	69.65
7	Phojet	6.87	6.87	4.97	1.82	79.48
14	Phojet	6.51	6.51	4.83	1.65	80.51

The purities for other triggers are defined in similar fashion. As an example, the purity for the ad hoc trigger definitions considered in eq. (4.1.4), eq. (4.1.7) and eq. (4.1.6) are given in eq. (4.4.7), eq. (4.4.8) and eq. (4.4.9), respectively.

$$\text{Purity}_{(\text{SD-R})} = \frac{eff_{\text{SD-R}} f_{\text{SD-R}}}{P^X_{\text{SD-L}} f_{\text{SD-L}} + P^X_{\text{SD-R}} f_{\text{SD-R}} + P^X_{\text{DD}} f_{\text{DD}} + P^X_{\text{CD}} f_{\text{CD}} + P^X_{\text{ND}} f_{\text{ND}}} \tag{4.4.7}$$

$$\text{Purity}_{(\text{CD})} = \frac{eff_{\text{CD}} f_{\text{CD}}}{P^X_{\text{SD-L}} f_{\text{SD-L}} + P^X_{\text{SD-R}} f_{\text{SD-R}} + P^X_{\text{DD}} f_{\text{DD}} + P^X_{\text{CD}} f_{\text{CD}} + P^X_{\text{ND}} f_{\text{ND}}} \tag{4.4.8}$$

$$\text{Purity}_{(\text{DD})} = \frac{eff_{\text{DD}} f_{\text{DD}}}{P^X_{\text{SD-L}} f_{\text{SD-L}} + P^X_{\text{SD-R}} f_{\text{SD-R}} + P^X_{\text{DD}} f_{\text{DD}} + P^X_{\text{CD}} f_{\text{CD}} + P^X_{\text{ND}} f_{\text{ND}}} \tag{4.4.9}$$

We can also calculate the minimum bias efficiency ($\text{Eff}^{\text{trigger X}}_{\text{MB}}$), i.e. the fraction of events of type X that the trigger-X selects from a minimum bias sample.

$$\text{Eff}^{\text{trigger X}}_{\text{MB}} = \frac{\#\text{ events in selected sample}}{\#\text{ total events in original minimum bias sample}} \tag{4.4.10}$$

For instance, the minimum bias efficiency of the ad hoc SD-L trigger can be written as:

$$\text{Eff}^{\text{SD-L}}_{\text{MB}} = \frac{eff_{\text{SD-L}} N_{\text{SD-L}} + P^{\text{SD-L}}_{\text{SD-R}} N_{\text{SD-R}} + P^{\text{SD-L}}_{\text{DD}} N_{\text{DD}} + P^{\text{SD-L}}_{\text{CD}} N_{\text{CD}} + P^{\text{SD-L}}_{\text{ND}} N_{\text{ND}}}{N_{\text{MB}}} \tag{4.4.11}$$

$$\mathrm{Eff}_{\mathrm{MB}}^{\text{SD-L}} = \mathit{eff}_{\text{SD-L}} f_{\text{SD-L}} + P_{\text{SD-R}}^{\text{SD-L}} f_{\text{SD-R}} + P_{\mathrm{DD}}^{\text{SD-L}} f_{\mathrm{DD}} + P_{\mathrm{CD}}^{\text{SD-L}} f_{\mathrm{CD}} + P_{\mathrm{ND}}^{\text{SD-L}} f_{\mathrm{ND}} \tag{4.4.12}$$

The probabilities P_Y^X are obtained analyzing a large number of single (left and right), double, central-diffractive (only for Phojet) and non diffractive events generated using standard Pythia6 and Phojet Monte Carlo generators.

There most be noted, however, that these Monte Carlo generators are not tuned for diffraction, so in the next section a convolution procedure is used to compensate for this in the calculation of the systematic uncertainty of single diffractive cross section.

In table 4.5 we show the integrated efficiencies (to pure events), the fraction of collected events from a minimum bias sample, and the purity (the percent of true events in the collected events from the minimum bias sample) reached by the ad hoc triggers defined in section 4.1.2. To produce this table we first compute the values separately for the case of Pythia6 and Phojet using their respective fractions. Then we show the average of both values and use their difference as an estimate of the systematic uncertainty. This of course can't be done in the case of the ad hoc trigger for central diffraction since Pythia6 does not include this process. In this case we only show the values calculated from Phojet.

For single diffraction SD-L we can see that the integrated efficiencies improved by a factor of 2.2 and 2.5 using two and four AD stations respectively. Furthermore, the purity of the collected sample also increases from 66.07% to 81.44 and 86.04%.

A similar picture is drawn for SD-R, the integrated efficiency increases by a factor of 1.6 by using two AD stations and by a factor of 1.8 when all the four AD stations are used. The purity also increases from 62.05% to 78.72% and 84.14% by using two and four AD stations respectively.

It is worth to note also that for both SD-L and SD-R the estimated systematic uncertainty in efficiency and purity decreases by the addition of the AD stations.

For double diffraction we see the efficiency to pure events increases by a factor of 3 and 3.7 when using two and four stations respectively. The purity is also enhanced. Nevertheless in this case, the systematic uncertainty increases by adding two and four stations.

For central diffraction the efficiency is very low using standard detectors and it remains almost constant by adding the AD stations (there is a very small decrease in the efficiency). However, there is a substantial gain in the purity of the collected sample. By adding two stations the purity increases by a factor of 1.4 to 97.2% which is almost a pure sample. Adding the other two station produces little further increase in purity.

In the case of the 1-arm-L selections we can see that the efficiency on pure SD-L diffractive events is enhanced by a factor of 1.5 an 1.7 by adding two and four AD stations. Similarly, the efficiency of 1-arm-R in selecting SD-R events increase by 1.3 and 1.4 with two and four stations. In both cases the purity increases from around 60% to around 75% and 80%. It is observed that the systematic uncertainty in the efficiency and purity drops as we extend the rapidity coverage by adding more AD stations.

Table 4.5: Trigger efficiencies and purity of selected sample for $\sqrt{s} = 7$ TeV for ad hoc triggers. The values are the average of Pythia6 and Phojet. The errors displayed represent the systematic uncertainty estimated from the difference between Pythia6 and Phojet (except for central diffraction since Pythia6 does not implement it). The sub-indexes are: 0 = no AD station, 1 = two stations and 2 = four stations

trigger	Efficiency Pure–events(%)	Efficiency Minimum–Bias (%)	Purity (%)
ad hoc triggers, $\sqrt{s} = 7$ TeV			
SD-L$_0$	12.19 ± 0.90	1.53 ± 0.29	66.07 ± 6.57
SD-L$_1$	26.92 ± 0.63	2.73 ± 0.52	81.44 ± 4.07
SD-L$_2$	31.22 ± 0.19	3.00 ± 0.59	86.04 ± 2.31
SD-R$_0$	18.15 ± 1.48	2.43 ± 0.48	62.05 ± 7.24
SD-R$_1$	29.89 ± 0.94	3.14 ± 0.62	78.72 ± 5.06
SD-R$_2$	33.09 ± 0.29	3.25 ± 0.62	84.14 ± 3.00
DD_0	5.10 ± 0.05	0.71 ± 0.29	61.72 ± 0.04
DD_1	15.37 ± 0.83	1.74 ± 0.80	77.52 ± 0.58
DD_2	19.18 ± 1.95	2.13 ± 1.05	80.60 ± 1.21
CD_0	3.28	0.09	65.72
CD_1	3.11	0.06	97.20
CD_2	3.10	0.06	98.73

Table 4.6: Trigger efficiencies and purity of selected sample for $\sqrt{s} = 14$ TeV for ad hoc triggers. The values are the average of Pythia6 and Phojet. The errors displayed represent the systematic uncertainty estimated from the difference between Pythia6 and Phojet (except for central diffraction since Pythia6 does not implement it). The sub-indexes are: 0 = no AD station, 1 = two stations and 2 = four stations

trigger	Efficiency Pure–events(%)	Efficiency Minimum–Bias (%)	Purity (%)
ad hoc triggers, $\sqrt{s} = 14$ TeV			
SD-L$_0$	11.13 ± 0.89	1.37 ± 0.25	63.67 ± 6.62
SD-L$_1$	25.01 ± 1.18	2.48 ± 0.43	78.50 ± 4.65
SD-L$_2$	29.41 ± 0.65	2.76 ± 0.50	83.03 ± 3.33
SD-R$_0$	16.47 ± 1.50	2.18 ± 0.42	59.30 ± 7.34
SD-R$_1$	27.68 ± 1.45	2.86 ± 0.53	75.53 ± 5.72
SD-R$_2$	30.99 ± 1.05	2.97 ± 0.53	81.32 ± 4.12
DD_0	4.56 ± 0.19	0.63 ± 0.26	61.08 ± 0.76
DD_1	13.86 ± 0.25	1.56 ± 0.69	76.27 ± 0.74
DD_2	17.65 ± 0.87	1.92 ± 0.89	79.75 ± 1.14
CD_0	2.80	0.07	65.66
CD_1	2.68	0.05	97.31
CD_2	2.68	0.04	98.97

The efficiency of the combined condition 2-arm and $\Delta\eta > 3$ in selecting pure double-diffractive events is, similarly to the ad hoc case, improved by a factor of 2.2 and 2.7, while there is little improvement on the purity of the collected events. In the case the estimated systematic uncertainty rises to about 4 percent for both purity and efficiency.

Table 4.7: Trigger efficiencies and purity of selected sample for $\sqrt{s} = 7$ TeV for 1-arm-L(R)/2-arm triggers. The values shown are the average of Pythia6 and Phojet. The errors displayed represent the systematic uncertainty estimated from the difference between Pythia6 and Phojet. The sub-indexes are: 0 = no AD station, 1 = two stations and 2 = four stations

trigger	Efficiency Pure–events(%)	Efficiency Minimum–Bias(%)	Purity (%)
1-arm-L(R)/2-arm, $\sqrt{s} = 7$ TeV			
1-arm-L $_0$	25.14 ± 1.69	3.31 ± 0.60	62.61 ± 5.26
1-arm-L $_1$	39.83 ± 1.39	4.18 ± 0.65	78.21 ± 2.03
1-arm-L $_2$	44.12 ± 0.56	4.36 ± 0.67	83.04 ± 0.08
1-arm-R $_0$	32.21 ± 2.47	4.69 ± 0.94	57.05 ± 6.44
1-arm-R $_1$	43.94 ± 1.91	4.82 ± 0.80	75.01 ± 3.46
1-arm-R $_2$	47.14 ± 1.25	4.79 ± 0.72	80.78 ± 1.09
2-arm $_0\Delta\eta > 3$ (DD)	15.23 ± 0.78	3.20 ± 1.33	40.83 ± 2.56
2-arm $_1\Delta\eta > 3$ (DD)	34.61 ± 2.57	5.53 ± 2.44	54.44 ± 2.85
2-arm $_2\Delta\eta > 3$ (DD)	42.05 ± 4.69	6.50 ± 2.93	56.41 ± 4.47

Table 4.8: Trigger efficiencies and purity of selected sample for $\sqrt{s} = 14$ TeV for 1-arm-L(R)/2-arm triggers. The values shown are the average of Pythia6 and Phojet. The errors displayed represent the systematic uncertainty estimated from the difference between Pythia6 and Phojet. The sub-indexes are: 0 = no AD station, 1 = two stations and 2 = four stations

trigger	Efficiency Pure–events(%)	Efficiency Minimum–Bias(%)	Purity (%)
1-arm-L(R)/2-arm, $\sqrt{s} = 14$ TeV			
1-arm-L $_0$	22.88 ± 1.48	2.98 ± 0.56	60.14 ± 5.51
1-arm-L $_1$	36.72 ± 1.75	3.77 ± 0.58	75.51 ± 2.97
1-arm-L $_2$	41.11 ± 1.21	3.97 ± 0.61	80.28 ± 1.57
1-arm-R $_0$	29.34 ± 2.26	4.24 ± 0.92	54.63 ± 7.22
1-arm-R $_1$	40.50 ± 2.21	4.37 ± 0.75	72.14 ± 4.63
1-arm-R $_2$	43.80 ± 1.81	4.35 ± 0.68	78.15 ± 2.69
2-arm $_0\Delta\eta > 3$ (DD)	13.85 ± 0.94	2.92 ± 1.21	40.26 ± 3.71
2-arm $_1\Delta\eta > 3$ (DD)	31.50 ± 2.19	5.05 ± 2.22	53.44 ± 3.43
2-arm $_2\Delta\eta > 3$ (DD)	38.67 ± 3.45	5.92 ± 2.68	56.27 ± 3.85

4.5 Estimation of systematic uncertainty on single diffractive cross section measurement

The strategy to calculate the cross section is to estimate the ratio $\sigma_{\mathrm{SD}}/\sigma_{\mathrm{INEL}}$ via the ratio of 1-arm-L(R) to 2-arm triggers, and then measure separately the total inelastic cross section σ_{INEL}. This procedure is similar to that used in the ALICE paper on diffraction [23].

The total number of events of a given process is the product of the integrated luminosity of the beam and the cross section σ for the process.

$$N = \mathscr{L}\sigma \tag{4.5.1}$$

However, experiments see only a fraction of that number due to efficiency and geometry constrains.

$$N_{\mathrm{seen}} = \mathscr{L}\sigma A \tag{4.5.2}$$

In order to identify if an event is diffractive or not, we defined offline triggers (see section 4.1.3) which are more likely to fire when the event belong to a certain class than to others. These are the 1-arm-L and 1-arm-R triggers, which are fired preferentially by diffractive events having the diffracted proton going to the left and right side of the ALICE experiment, respectively. We also defined the 2-arm triggers, which fire preferentially on non single diffractive events (double diffractive, central diffractive and non diffractive).

In order to get the real number of events from the number of events seen by a particular trigger we need to estimate two important characteristics: The purity and efficiency of the trigger.

As seen in section 4.4, the efficiency of a trigger tell us what percent of the events is selected by the trigger from a given initial sample. The purity instead, give the fraction of events that are of the right type in the selected sample, i.e., after the initial sample has been analyzed by the trigger.

In the previous section, these values where computed but the Monte Carlo generators used where not tuned for diffraction. Here we correct them by a convolution process explained below.

A suitable number of single (left and right), double, central diffractive (only for Phojet) and non diffractive events are generated using standard Pythia6 and Phojet Monte Carlo generators.

The particles from these events are transported through the complete ALICE geometry by AliRoot. After the transport, the hits of the particles in the sensitive elements of the detectors are analyzed in order to tag the event as 1-arm-L, 1-arm-R or 2-arm.

If the event analyzed is SD-L or SD-R, the diffracted mass M_X of the event is computed from the Monte Carlo information and the efficiency of the triggers become a function of M_X (see fig. 4.2).

Then, these efficiency curves are convoluted with a model describing the production of single-diffracted events as function of the diffracted mass. The model is normalized in the range from 1.08 (lower production threshold, sum of proton and π_0 mass) to 200 GeV/c^2. This procedure gives the mean efficiency of the trigger according to a particular election of Monte Carlo generator an diffractive model.

There are several models describing production of single-diffracted events. Nevertheless, it is possible to account for the differences among models by choosing two curves as upper and lower bounds. Here we use the Kaidalov-Poghosyan model (KP) to estimate the central value, and a ±50% variation of this model, as upper and lower bound for the different single-diffractive models, and as a measure of the systematic uncertainty in the knowledge of diffractive production. Additionally we also used the Donnachie-Landshoff model.

To get the ±50% variation, we multiplied the KP model curve by two linear functions, f_+ and f_-, of the form $f(x) = ax + b$ defined in the range $1.08 \leq x \geq 200$. The end points of this functions are:

$$f_+(x) = \begin{cases} 1.0 & \text{if } x = 1.08 \\ 1.5 & \text{if } x = 200 \end{cases} \qquad f_-(x) = \begin{cases} 1.0 & \text{if } x = 1.08 \\ 0.5 & \text{if } x = 200 \end{cases} \tag{4.5.3}$$

Afterwards, we re-normalize the resulting curves, obtaining KP+50% and KP−50% model variations. The different normalized models can be seen in fig. 4.7, super imposed to the efficiency curves as function of diffracted mass.

The efficiencies of the 1-arm-L(R)/2-arm and their systematic uncertainties, estimated as explained above, are shown in table 4.9. We first show the values when no AD's are considered. This is done as a crosscheck and they are found to be in good agreement with where those obtained in [23]. Then, we shown the values when the ADA and ADC are included.

With the mean efficiency of each trigger, according to each combination of generator and diffractive model (eight combinations), and knowing the fractions that each generator assigns to each different process, it is possible to compute the purity of sample, selected by the trigger, from a minimum bias sample.

Then, having the efficiency and purity of each trigger (according to a particular combination of model and Monte Carlo generator) we can calculate the

Figure 4.7: Efficiency of 1-arm-L (left) and 1-arm-R (right) offline selections vs M_X. Solid red and blue lines represent current situation. Dashed red and blue lines shows the situation when ADA and ADC are included in the analysis. Simulations where done with Pythia6 (blue) and Phojet (red). The other lines show the different models used to estimate systematic uncertainty in the mean efficiency.

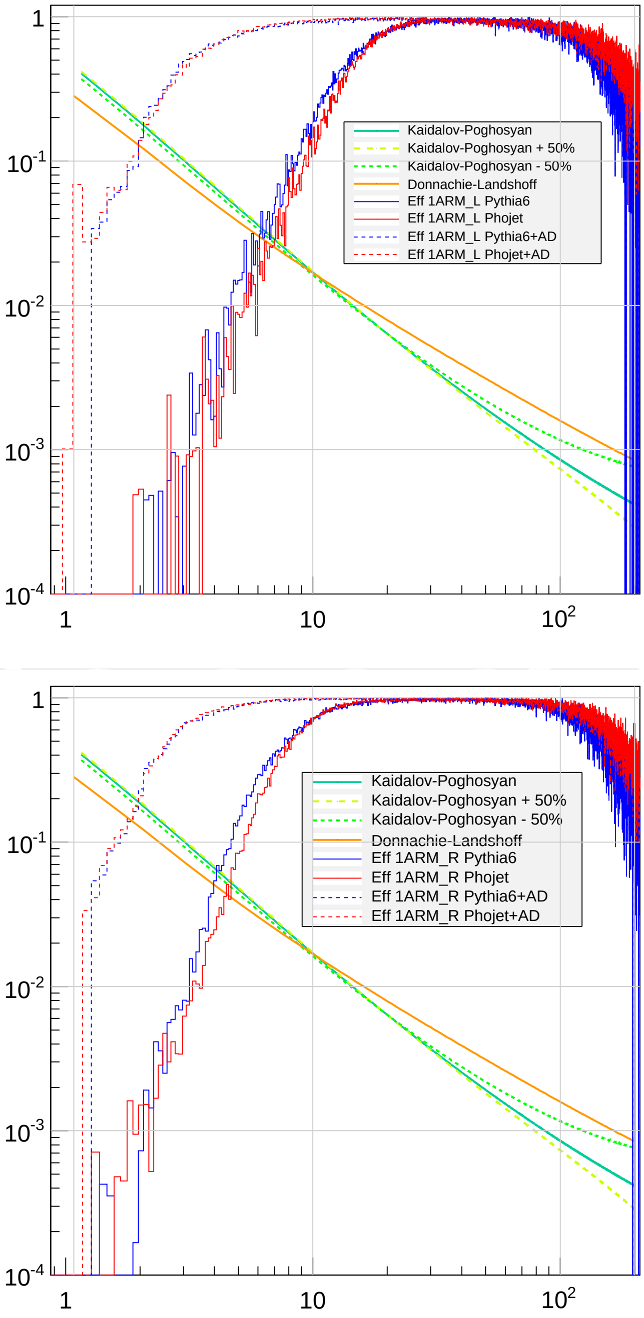

number of total events produced in the proton-proton collisions (N_{total}) from the number of events seen by the trigger (N_{seen}), in the following way.

First we calculate the number of true events in our selected sample: $N_{\text{true}} = N_{\text{seen}} \times \text{purity}$. Now we have the number of events of the right type seen by the trigger, from this we can extrapolate to the total number of events produced.

$$N_{\text{total}} = N_{\text{true}}/\text{eff}_{\text{trigg}} = \frac{(N_{\text{seen}} \times \text{purity})}{\text{eff}_{\text{trigg}}} \tag{4.5.4}$$

Then we can take the ratios of single-diffractive to non-single-diffractive (NSD) events:

$$\frac{\sigma_{\text{SD}}}{\sigma_{\text{NSD}}} = \frac{N^{\text{total}}_{\text{SD-L}} + N^{\text{total}}_{\text{SD-R}}}{N^{\text{total}}_{\text{NSD}}} \tag{4.5.5}$$

$$\frac{\sigma_{\text{SD}}}{\sigma_{\text{NSD}}} = \frac{\dfrac{N^{\text{trigg}}_{\text{1-arm-L}} \times \text{Purity}^{\text{1-arm-L}}_{\text{SD-L}}}{\text{Efficiency}^{\text{1-arm-L}}_{\text{SD-L}}} + \dfrac{N^{\text{trigg}}_{\text{1-arm-R}} \times \text{Purity}^{\text{1-arm-R}}_{\text{SD-R}}}{\text{Efficiency}^{\text{1-arm-R}}_{\text{SD-R}}}}{\dfrac{N^{\text{trigg}}_{\text{2-arm}} \times \text{Purity}^{\text{2-arm}}_{\text{NSD}}}{\text{Efficiency}^{\text{2-arm}}_{\text{NSD}}}} \tag{4.5.6}$$

Using the results from previous section we have that the percent of SD-L (SD-R) events in a sample selected by the 1-arm-L (1-arm-R) trigger estimated using efficiencies from a given model are:

$$\text{Purity}^{\text{1-arm-L}}_{\text{SD-L}} = \frac{\text{eff}^{\text{1-arm-L}}_{\text{SD-L}} \times f_{\text{SD-L}}}{\text{eff}^{\text{1-arm-L}}_{\text{SD-L}} f_{\text{SD-L}} + \text{eff}^{\text{1-arm-L}}_{\text{SD-R}} f_{\text{SD-R}} + \text{eff}^{\text{1-arm-L}}_{\text{NSD}} f_{\text{NSD}}} \tag{4.5.7}$$

$$\text{Purity}^{\text{1-arm-R}}_{\text{SD-R}} = \frac{\text{eff}^{\text{1-arm-R}}_{\text{SD-R}} \times f_{\text{SD-R}}}{\text{eff}^{\text{1-arm-R}}_{\text{SD-L}} f_{\text{SD-L}} + \text{eff}^{\text{1-arm-R}}_{\text{SD-R}} f_{\text{SD-R}} + \text{eff}^{\text{1-arm-R}}_{\text{NSD}} f_{\text{NSD}}} \tag{4.5.8}$$

Table 4.9: Efficiency of 1-arm-L, 1-arm-R and 2-arm trigger to single diffractive and non single diffractive events. The first three data rows are for the current situation in which the triggers use information from VZERO, SPD and FMD detectors. The next three rows shows the case when the triggers are improved with information from the AD counters.

	Process	1-arm-L	1-arm-R	2-arm
No ADs	SD L-side	$0.235^{+0.120}_{-0.0145}$	$0.0007^{+0.0008}_{-0.0002}$	$0.036^{+0.038}_{-0.009}$
	SD R-side	$0.0003^{+0.0002}_{-0.0001}$	$0.338^{+0.125}_{-0.014}$	$0.032^{+0.036}_{-0.009}$
	NSD	$0.013^{+0.007}_{-0.007}$	$0.023^{+0.01}_{-0.01}$	$0.952^{+0.027}_{-0.027}$
ADA + ADC	SD L-side	$0.551^{+0.082}_{-0.009}$	$0.00050^{+0.00006}_{-0.00006}$	$0.037^{+0.038}_{-0.009}$
	SD R-side	$0.00012^{+0.00018}_{-0.00004}$	$0.624^{+0.076}_{-0.012}$	$0.032^{+0.035}_{-0.009}$
	NSD	$0.009^{+0.006}_{-0.006}$	$0.012^{+0.008}_{-0.008}$	$0.976^{-0.015}_{+0.015}$

And the purity of the 2-arm trigger with respect to non single diffractive (NSD) events is:

$$\text{Purity}^{\text{2-arm}}_{\text{NSD}} = \frac{\text{eff}^{\text{2-arm}}_{\text{NSD}}\, f_{\text{NSD}}}{\text{eff}^{\text{2-arm}}_{\text{SD-L}}\, f_{\text{SD-L}} + \text{eff}^{\text{2-arm}}_{\text{SD-R}}\, f_{\text{SD-R}} + \text{eff}^{\text{2-arm}}_{\text{NSD}}\, f_{\text{NSD}}} \tag{4.5.9}$$

The trigger efficiencies to non-single diffractive (NSD) processes are:

$$\text{eff}^{\text{1-arm-L}}_{\text{NSD}}\, f_{\text{NSD}} = \text{eff}^{\text{1-arm-L}}_{\text{DD}}\, f_{\text{DD}} + \text{eff}^{\text{1-arm-L}}_{\text{CD}}\, f_{\text{CD}} + \text{eff}^{\text{1-arm-L}}_{\text{ND}}\, f_{\text{ND}} \tag{4.5.10}$$

$$\text{eff}^{\text{1-arm-R}}_{\text{NSD}}\, f_{\text{NSD}} = \text{eff}^{\text{1-arm-R}}_{\text{DD}}\, f_{\text{DD}} + \text{eff}^{\text{1-arm-R}}_{\text{CD}}\, f_{\text{CD}} + \text{eff}^{\text{1-arm-R}}_{\text{ND}}\, f_{\text{ND}} \tag{4.5.11}$$

$$\text{eff}^{\text{2-arm}}_{\text{NSD}}\, f_{\text{NSD}} = \text{eff}^{\text{2-arm}}_{\text{DD}}\, f_{\text{DD}} + \text{eff}^{\text{2-arm}}_{\text{CD}}\, f_{\text{CD}} + \text{eff}^{\text{2-arm}}_{\text{ND}}\, f_{\text{ND}} \tag{4.5.12}$$

And the fraction of NSD events is:

$$f_{\text{NSD}} = f_{\text{DD}} + f_{\text{CD}} + f_{\text{ND}} \tag{4.5.13}$$

$f_{\text{SD-L}}$, $f_{\text{SD-R}}$, f_{DD}, f_{CD} and f_{ND} represent the fraction of events of each type (single diffractive on left and right side, double diffractive, central diffractive and non diffractive)in the minimum bias sample. But these fractions are in turn:

$$f_{\text{SD-L}} = \tfrac{1}{2}\sigma_{\text{SD}}/\sigma_{\text{INEL}} \tag{4.5.14}$$

$$f_{\text{SD-R}} = \tfrac{1}{2}\sigma_{\text{SD}}/\sigma_{\text{INEL}} \tag{4.5.15}$$

$$f_{\text{DD}} = \sigma_{\text{DD}}/\sigma_{\text{INEL}} \tag{4.5.16}$$

$$f_{\text{CD}} = \sigma_{\text{CD}}/\sigma_{\text{INEL}} \tag{4.5.17}$$

$$f_{\text{ND}} = \sigma_{\text{ND}}/\sigma_{\text{INEL}} \tag{4.5.18}$$

Putting it all together and calling $x = \sigma_{\text{SD}}/\sigma_{\text{NSD}}$ we have:

$$\begin{aligned} x = \frac{1}{2} \times \text{Ratio}^{\text{1-arm-L}}_{\text{2-arm}} \times \frac{\frac{1}{2}\left(\text{eff}^{\text{2-arm}}_{\text{SD-L}} + \text{eff}^{\text{2-arm}}_{\text{SD-R}}\right) x + \text{eff}^{\text{2-arm}}_{\text{NSD}}}{\frac{1}{2}\left(\text{eff}^{\text{1-arm-L}}_{\text{SD-L}} + \text{eff}^{\text{1-arm-L}}_{\text{SD-R}}\right) + \text{eff}^{\text{1-arm-L}}_{\text{NSD}}/x} + \\ \frac{1}{2} \times \text{Ratio}^{\text{1-arm-R}}_{\text{2-arm}} \times \frac{\frac{1}{2}\left(\text{eff}^{\text{2-arm}}_{\text{SD-L}} + \text{eff}^{\text{2-arm}}_{\text{SD-R}}\right) x + \text{eff}^{\text{2-arm}}_{\text{NSD}}}{\frac{1}{2}\left(\text{eff}^{\text{1-arm-R}}_{\text{SD-L}} + \text{eff}^{\text{1-arm-R}}_{\text{SD-R}}\right) + \text{eff}^{\text{1-arm-R}}_{\text{NSD}}/x} \end{aligned} \tag{4.5.19}$$

This makes the calculation of x a recursive problem so a few iterations are needed before reaching final values. From $x = \sigma_{\text{SD}}/\sigma_{\text{NSD}}$ (since $\sigma_{\text{INEL}} = \sigma_{\text{SD}} + \sigma_{\text{NSD}}$) we obtain the ratio of single to inelastic cross section: $\sigma_{\text{SD}}/\sigma_{\text{INEL}} = x/(x+1)$. Since this value depends on the generator and model used we have eight possible values for the $\sigma_{\text{SD}}/\sigma_{\text{INEL}}$ ratio. We use KP model for the central value taking the average of Pythia6 and Phojet. We pick the minimum and maximum among the eight values to estimate the systematic uncertainties.

Using the measured values from the paper for the ratio of 1-arm-L(R) to 2-arm triggers and only VZERO, SPD and FMD detectors (No AD case) we obtain:

$$\sigma_{\text{SD}}/\sigma_{\text{INEL}} = 0.20^{+0.05}_{-0.08} \tag{4.5.20}$$

Which is in good agreement with the measurement reported in the paper:

$$\sigma_{\mathrm{SD}}/\sigma_{\mathrm{INEL}} = 0.20^{+0.04}_{-0.07} \tag{4.5.21}$$

Now we repeat the procedure considering this time the efficiency curves of the triggers when the AD stations are included in the analysis (ADA and ADC). The only missing piece is the ratio of 1-arm-L(R) to 2-arm triggers which, as expected, will not be the same as in the no AD case. We extrapolate its value from the efficiencies values, using the fact that the value of the SD cross section is independent of the setup used to measure it.

Doing this we predict that the systematic uncertainty, in the measurement of the ratio $\sigma_{\mathrm{SD}}/\sigma_{\mathrm{INEL}}$, when using the ADA and ADC stations, in addition to the VZERO, SPD and FMD detectors, will be:

$$\sigma_{\mathrm{SD}}/\sigma_{\mathrm{INEL}} = 0.20^{+0.02}_{-0.03} \tag{4.5.22}$$

Which represent a reduction by approximately a factor of two, with respect to the current situation (no AD stations), on the systematic uncertainty associated with our knowledge of single diffractive processes.

Chapter 5

Conclusions

We have presented a study of the performance of a new array of scintillator stations designed to improve the sensitivity of ALICE to diffractive events.

The two AD stations closest to the nominal interaction point are located behind the muon spectrometer and their shielding structures in the C-side (or left side) and behind a compensator magnet on the A-side (or right side). The other two stations are located behind even more structures. As a consequence, each time a collision occur, there is a big amount of secondaries reaching the scintillators from the surrounding structures such as the beam pipe and shielding elements. Some secondaries came even from structures behind the scintillators (backscattering). This however, can play in favor of the efficiency of the stations. By tracing back those tracks to the physical primaries from where they are produced, we see that pseudorapidity of the primaries keeps some correlation with the geometrical acceptance of the detector. Some of the primaries that give birth to secondaries eventually reaching the AD stations have even a larger pseudorapidity (in absolute value) than that of the corresponding AD station, and will not make otherwise a hit on the detector without the help of their secondaries. This has the effect of making the AD station sensible to lower diffracted masses. In the case when the primary as a lower pseudorapidity (i.e. a more central track) than the geometrical acceptance of the AD station, the other detectors (SPD, FMD and VZERO) participating in the online trigger or offline selection can veto the event, minimizing the otherwise negative impact of this effect.

Beam gas interactions is the largest source of background in the ALICE environment. Although not studied in this work, it can be highly suppressed by requiring all particles to arrive in appropriate time windows, in coincidence with the bunch crossing. If particles in the event arrive outside this window then they most probably come from beam-gas interaction, and the event should not be stored (or marked as beam-gas). This time window scheme is used for the VZERO detectors in ALICE (which also uses scintillators)

In order for the offline analysis to profit from the information given by the AD stations, it is mandatory to include this stations in the data taking decision. The more flexible way to do this is by defining minimum bias triggers with extended rapidity coverage. Since the minimum bias triggers already selects almost all the non diffractive events (which comprises the largest fraction of the minimum bias events) this will not suppose an excessive increase in the trigger rates and will make accessible to the offline analysis low diffracted masses event that would be otherwise lost for ever.

Provided that we use the AD system helping in the data taking decision via for example the extension of the minimum bias triggers, we can achieve a big improvement in the offline analysis of diffractive events.

In particular, we have shown that using the information from these stations in the event selection employed in a recent paper of the ALICE collaboration [23] we can increase the efficiency in the collection of diffractive events by a factor of up to 1.5 in the case of SD-L events.

Furthermore, the purity of the collected sample increase from about 62 (57) percent to up to 83 (80) percent for SD-L (SD-R) events.

This boost of the efficiency is driven by the improved performance in collecting events with low diffracted masses which in turn is due to the increase in the rapidity coverage delivered by these stations.

In addition, we have also shown ad hoc triggers that can be used as online trigger or in offline analysis. Due to the stricter rapidity cuts in their definition (which makes them less sensible to high diffracted masses), their efficiency is not as high as the 1-arm-L/1-arm-R selections, although their purity is similar.

For central diffraction, the use of the ad hoc trigger with the AD stations improves dramatically the purity of the collected events (from a minimum bias sample) in comparison to the case where only standard ALICE detectors are used without having a negative impact on the efficiency (which is evidently low).

Finally, we have shown how the inclusion of ADA and ADC stations in the MB-OR and 1-arm-L(R)/2-arm triggers will reduce the systematic uncertainty in the measurement of the cross section ratio $\sigma_{\mathrm{SD}}/\sigma_{\mathrm{INEL}}$.

Bibliography

[1] Performance of the alice v0 system. Technical Report CERN-PH-EP-2013-082, CERN, Geneva, Apr 2013.

[2] F. Abe et al. Measurement of $p\ ^{-}\ p$ single diffraction dissociation at $\sqrt{}\ s$ =546 and 1800 gev. *Phys. Rev. D*, 50:5535–5549, Nov 1994.

[3] ALICE Collaboration and B Alessandro and F Antinori and J A Belikov and C Blume and A Dainese and P Foka and P Giubellino and B Hippolyte and C Kuhn and G and M Monteno and A Morsch and T K Nayak and J Nystrand and M López Noriega and G Paić and J Pluta and L Ramello and J-P Revol and K Šafařík and J Schukraft and Y Schutz and E Scomparin and R Snellings and O Villalobos Baillie and E Vercellin. Alice: Physics performance report, volume ii. *Journal of Physics G: Nuclear and Particle Physics*, 32(10):1295, 2006.

[4] Vincenzo Barone and Enrico Predazzi. *High-Energy Particle Diffraction*. Springer, second edition edition, 2002.

[5] Gerhard Baur, Kai Hencken, Dirk Trautmann, Serguei Sadovsky, and Yuri Kharlov. Coherent and a interactions in very peripheral collisions at relativistic ion colliders. *Physics Reports*, 364(5):359 – 450, 2002.

[6] ALICE Collaboration, F Carminati, P Foka, P Giubellino, A Morsch, G Paic, J-P Revol, K Safarík, Y Schutz, and U A Wiedemann. Alice: Physics performance report, volume i. *Journal of Physics G: Nuclear and Particle Physics*, 30(11):1517, 2004.

[7] The ALICE Collaboration. The alice experiment at the cern lhc. *Journal of Instrumentation*, 3(08):S08002, 2008.

[8] R. Engel, M.A. Braun, C. Pajares, and J. Ranft. Diffraction dissociation, an important background to photon - photon collisions via heavy ion beams at LHC. *Z.Phys.*, C74:687–697, 1997.

[9] M. L. Good and W. D. Walker. Diffraction dissociation of beam particles. *Phys. Rev.*, 120:1857–1860, Dec 1960.

[10] K. Goulianos. Diffractive interactions of hadrons at high energies. *Physics Reports*, 101(3):169 – 219, 1983.

[11] K. Hencken, G. Baur, U. Dreyer, and D. Trautmann. Ultraperipheral Collisions. *ArXiv High Energy Physics - Phenomenology e-prints*, March 2005.

[12] Spencer R. Klein, Joakim Nystrand, and Ramona Vogt. Heavy quark photoproduction in ultraperipheral heavy ion collisions. *Phys. Rev. C*, 66:044906, Oct 2002.

[13] Konrad Kleinknecht. *detectors for particle radiation*. CAMBRIDGE, 1998.

[14] Louis Lyons. *Statistics for nuclear and particle physicists*. CAMBRIDGE, 1999.

[15] A. D. Martin. Summary Talk: First Workshop on Forward Physics and Luminosity Determination at the LHC. *ArXiv High Energy Physics - Phenomenology e-prints*, March 2001.

[16] J. Nystrand. Ultra-peripheral collisions of heavy ions at rhic and the lhc.

[17] J. Nystrand. Electromagnetic interactions in nucleus-nucleus and proton-proton collisions. *Nuclear Physics A*, 752(0):470 – 479, 2005. Proceedings of the 22nd International Nuclear Physics Conference (Part 2).

[18] J. Nystrand. Photoproduction in Ultra-Peripheral Heavy-Ion Collisions. *Nuclear Physics B Proceedings Supplements*, 184:146–151, November 2008.

[19] Torbj orn Sj ostrand, Stephen Mrenna, and Peter Skands. Pythia 6.4 physics and manual. *Journal of High Energy Physics*, 2006(05):026, 2006.

[20] Raimond Snellings. Elliptic flow: a brief review. *New Journal of Physics*, 13(5):055008, 2011.

[21] The ALICE Collaboration. Elliptic flow of charged particles in pb-pb collisions at $\sqrt{s_{NN}} = 2.76$ TeV. *Phys. Rev. Lett.*, 105:252302, Dec 2010.

[22] The ALICE Collaboration. Suppression of charged particle production at large transverse momentum in central pb–pb collisions at. *Physics Letters B*, 696(1–2):30 – 39, 2011.

[23] The ALICE Collaboration. Measurement of inelastic, single- and double-diffraction cross sections in proton–proton collisions at the LHC with ALICE. *ArXiv e-prints*, August 2012.

[24] The ALICE Collaboration. Pion, kaon, and proton production in central pb-pb collisions at $\sqrt{s_{\mathrm{NN}}}$=2.76 TeV. *Phys. Rev. Lett.*, 109:252301, Dec 2012.

[25] The ALICE Collaboration. Charge separation relative to the reaction plane in pb-pb collisions at $\sqrt{s_{NN}}$=2.76 TeV. *Phys. Rev. Lett.*, 110:012301, Jan 2013.

[26] The ALICE Collaboration. Coherent photoproduction in ultra-peripheral pb–pb collisions at. *Physics Letters B*, 718(4–5):1273 – 1283, 2013.

[27] The ALICE Collaboration. Transverse momentum distribution and nuclear modification factor of charged particles in p+Pb collisions at $\sqrt{s_{NN}}$=5.02 TeV. *Phys. Rev. Lett.*, 110:082302, Feb 2013.

[28] R. Vogt. Jet Photoproduction in Peripheral Heavy-Ion Collisions. *ArXiv High Energy Physics - Phenomenology e-prints*, July 2004.